Hardware Modification Free Active 3D-Drift Correction in Single-Molecule Localization Microscopy (SMLM)

Model-Based Control of a Super Resolution Microscope

K.E. Blokhuis

Master of Science Thesis

Delft University of Technology

Delft Center for Systems and Control

Hardware Modification Free Active 3D-Drift Correction in Single-Molecule Localization Microscopy (SMLM)

Model-Based Control of a Super Resolution Microscope

Master of Science Thesis

For the degree of Master of Science in Systems and Control at Delft University of Technology

K.E. Blokhuis

August 20, 2025

Faculty of Mechanical Engineering (ME) · Delft University of Technology

Abstract

Single-molecule localization microscopy (SMLM) enables imaging at nanometer-scale resolution but is highly sensitive to sample drift. Here, I present a live 3D drift correction approach that uses only fiducial markers and does not require any hardware modifications. The method uses fluorescent light from fiducial markers, extracted directly from the main imaging camera during acquisition. Using the computationally efficient Phasor approach to estimate the 3D-position of the beads [26], the control bandwidth is mostly limited by the maximum frame rate of the camera during acquisition (e.g. rates of >22 Hz at 25 fps). In addition, a system identification framework is proposed to identify drift dynamics, enabling the implementation of an optimal model-based control strategy. Experiments reached closed-loop stability with a precision of 0.6 nm in lateral direction and 2.4 nm in axial direction, showing the potential of the hardware-free drift correction approach.

Table of Contents

Preface

At seventeen years old, my journey at Delft University of Technology began, and with this thesis, it now comes to an end. When I first set foot on campus, I had no prior experience with engineering. I was amazed by how many students had already dismantled a microwave oven, a TV screen, or a vacuum cleaner. Now, with a BSc in Mechanical Engineering and an MSc in Systems & Control, I still haven't taken apart many household appliances, but I no longer feel intimidated by the idea. I suppose that's part of becoming an engineer.

For the final part of this journey, I'm grateful to Assoc. Prof. Smith for introducing me to the world of optics and for offering me the opportunity to work on my thesis in his lab, an experience that allowed me to further develop hands-on skills in the field of Systems & Control.
Special thanks go to MSc. Liam Cools for the many fruitful discussions we had regarding the design of the novel framework presented in this thesis. His guidance in optics and consistent, constructive feedback throughout the process have been incredibly helpful.
Collaborating with Dr. Dimitri Kromm was another highlight of this thesis. The optical setup designed by him, was made available to me throughout my research, and along the way, I learned more from him about optics than I could have hoped for. He generously answered all my questions, often accompanied by inspiring stories from his own research journey.
I would also like to thank Asst. Prof. Roderick Tas for his support in the lab, particularly with the preparation of biological samples, and for sharing his expertise in cellular structures and mechanics. His knowledge and motivation encouraged me to develop the solutions in this thesis to the best of my ability.
Furthermore, I would like to express my appreciation to Assoc. Professor A. Accardo and all those mentioned above for taking the time to read and evaluate my work.

Finally, I would like to thank all my friends that have listened to my endless stories during every step of my thesis. Great gratitude goes out to my parents and my brother helping me push through even when my motivation seemed to drift along the bottom of De Rotte, and to my girlfriend Vilte; Labai ačiū už jūsų palaikymą, meilę ir ypač už nustatytus terminus, kurių negalėjau išvengti.

Delft, University of Technology K.E. Blokhuis
August 20, 2025

“Vorming is datgene wat overblijft als je alles bent vergeten wat je geleerd hebt.”
— *Hendrikus Cornelis Blokhuis*

Glossary

List of Acronyms

CMOS	Complementary Metal-Oxide-Semiconductor
CRLB	Cramér-Rao Lower Bound
FOV	Field of View
LQG	Linear Quadratic Gaussian
LQR	Linear Quadratic Regulator
LTI	Linear Time Invariant
MLE	Maximum Likelihood Estimation
NP	Nano Particle
N4SID	Numerical Algorithms for Subspace State Space System Identification
PBSID$_{opt}$	Predictor-Based Subspace IDentification optimal
PSF	Point Spread Function
SMLM	Single-Molecule Localization Microscopy
SNR	Signal-to-Noise Ratio
SRM	Super Resolution Microscopy

Chapter 1

Introduction

For centuries, light microscopy has been a cornerstone of biological research, allowing scientists to observe cells and tissues in unprecedented detail. Traditional optical microscopes rely on visible light to form images, revealing structures such as nuclei, organelles, and larger protein assemblies. However, the resolution of conventional light microscopy is fundamentally limited by the diffraction of light, which restricts the smallest distinguishable features to roughly half the wavelength of the light used, typically around 200–300 nm.

Super Resolution Microscopy (SRM) has enabled researchers to reach resolutions far past the diffraction limit of standard optical microscopy. The research in SRM started in 1992 with the 4Pi concept, designed by Stefan Hell and Ernst Stelzer [18]. In the past three decades, research has been thriving with its pinnacle of Hell being awarded a Nobel Prize in chemistry in 2014 for the development of super-resolved fluorescence microscopy. During this period, several techniques have been designed to perform SRM for the specific needs of biologists and microscopists [35]. The best-known methods can be divided into three groups: stimulated emission depletion [11], structured illumination microscopy [13] and Single-Molecule Localization Microscopy (SMLM) [3][20][34][17].

SMLM provides researchers with the ability to visualize subcellular structures at nanometer resolution. For example, SMLM has been used to visualize the actin cytoskeleton, a network of protein filaments that supports the cell's shape and internal structure. Actin filaments are highly dynamic: they continuously grow and shrink, particularly in thin, sheet-like protrusions at the front of moving cells, called lamellipodia [7]. This dynamic remodeling generates the forces that push the cell forward, allowing it to move, a process essential for wound healing, immune responses, and other cellular activities. By imaging these filaments in three dimensions at a resolution below 20 nm [47], SMLM provides insight into the cellular mechanics that drives this locomotion [32]. Beyond structural imaging, SMLM has also become a powerful tool for quantitative studies: various analysis approaches have been developed to extract information about the distribution, size, shape and spatial organization of macromolecular complexes [46, 28].

In SMLM, maintaining a stable focal point over long acquisition times is essential to achieve high-resolution image reconstruction. This challenge naturally lends itself to the field of Systems & Control, as the microscope stage must be actively actuated to stabilize focus drift despite uncertainty and noise in the system dynamics, by using a Kalman Filter for state estimation and optimal control in the form of Linear Quadratic Regulator (LQR). The goal is schematically illustrated in Figure 1-1, which shows the closed-loop control structure of the super-resolution microscope. In this thesis, we explore the current state of drift compensation methods, present an improved approach to real-time drift correction, and outline future directions to further enhance drift stability in SMLM.

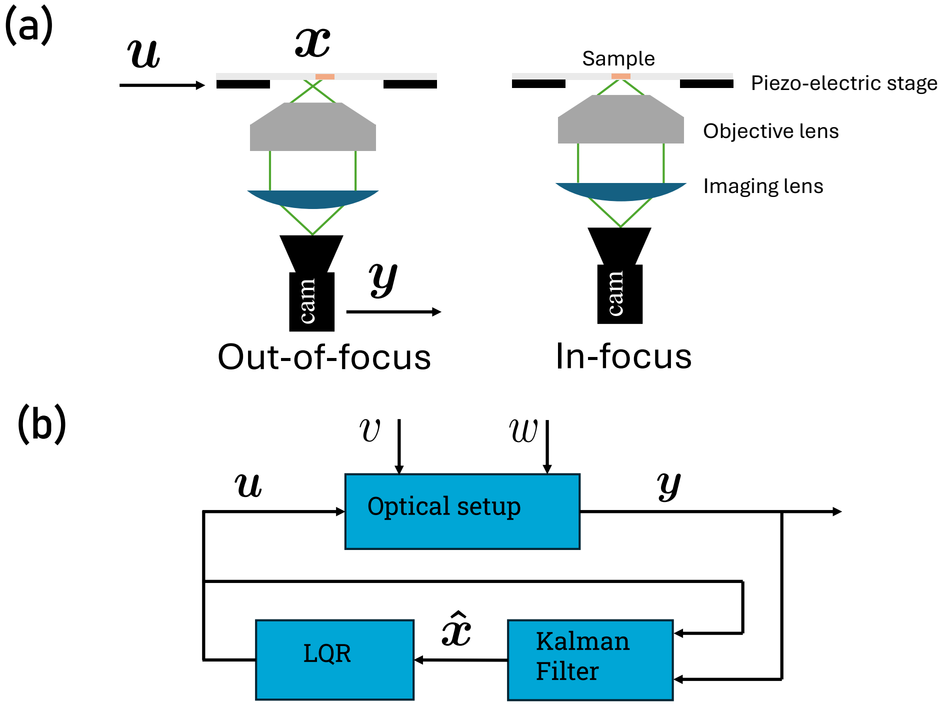

Figure 1-1: Schematic representation of the control objective: stabilization of the focal point in a super-resolution microscope. (a) Simplified schematic of the microscope setup, where the control input $\boldsymbol{u}$ is applied to an piezoelectric stage, the output $\boldsymbol{y}$ is derived from camera images, and the system states $\boldsymbol{x}$ represent the axial focus position. (b) Block diagram illustrating the closed-loop control architecture. A Kalman filter is used to optimally estimate the state $\boldsymbol{x}$ based on the control input $\boldsymbol{u}$, the measurements $\boldsymbol{y}$, and the statistical properties of the process noise w and measurement noise v. Subsequently, a LQR computes the optimal control input $\boldsymbol{u}$ based on the estimated state vector, $\hat{\boldsymbol{x}}$.

1-1 Background

SMLM relies on the principle that the positions of individual fluorescent molecules can be precisely determined as long as the Point Spread Function (PSF) do not overlap. When a fluorophore's position shifts by less than a pixel, the resulting changes in the intensity distribution across pixels are predictable, allowing for accurate calculation of its location. The precision with which a molecule can be localized depends on the distribution of its repeated localizations if it were imaged multiple times. This precision is primarily determined by the Signal-to-Noise Ratio (SNR) and the theoretically highest achievable precision given an

Maximum Likelihood Estimation (MLE) and given experimental parameters can be found using the Cramér-Rao Lower Bound (CRLB) [29]. To prevent PSF overlap, the emissions from different molecules are separated over time. This temporal separation is usually achieved through a process called photoswitching, where fluorescent molecules randomly switch between an "ON" (bright) state, where they emit light, and an "OFF" (dark) state, where they remain non-fluorescent. Photoswitching for any given molecule is random, so under optimal conditions only a few molecules will be in the ON state at any given moment, which ensures that their PSFs remain spatially distinct and do not overlap. This switching behavior causes the fluorophores to blink between bright and dark states. To capture all the molecules in a given Field of View (FOV), thousands of images are acquired in sequence. Over these many frames, each molecule ideally transitions to the ON state at least once. The images are then processed computationally to identify which molecules are in the ON state and to calculate their exact positions. Finally, the positions of all localized molecules from all frames are compiled into a single, high-resolution image, allowing the detailed reconstruction of the sample at a resolution beyond the limits of conventional light microscopy.

A big challenge in SMLM is sample drift relative to the objective during image acquisition. If this drift is not addressed, small movements can lead to blurred reconstructed images. To mitigate this, drift can be measured in multiple ways, which mostly all fall under three primary categories: image reconstruction-based, beam-based and fiducial marker-based drift identification. In image reconstruction-based drift identification, drift can be estimated directly from single-molecule localizations using for instance image cross-correlation [44]. However, this set of drift identification approaches require careful handling as the drift can only be compensated for in post-processing. This prohibits live compensation of the z-drift, for which the resolution drop cannot be restored. Moreover, some of the image reconstruction-based drift identification methods are only able to provide drift estimation in x- and y-direction. Beam-based methods enable real-time drift estimation by analyzing the interaction of laser light with the sample or sample plane. Examples include speckle pattern tracking, secondary laser reflection systems such as Nikon Perfect Focus, and engineered PSFs like astigmatic or double-helix designs that allow extraction of the z-position from PSF deformations [1, 6, 21, 33, 43]. While these approaches allow live z-drift compensation, they require substantial optical modifications, additional lasers, sensors, or moving parts, which can complicate integration with commercial microscopes. Finally, fiducial marker-based techniques use fluorescent beads or gold nano-particles as markers to act as a reference point on the sample plane [26, 10, 25]. These markers can be tracked to determine the drift. Subsequently, active control algorithms can dynamically compensate for the detected drift in real-time.

Currently, these control techniques rely on "simple" PID algorithms [10], which provide sub-optimal drift correction. In [37], the importance of high-precision drift correction is emphasized, as even nanometer-scale movements can mislocalize single-molecule positions. Over long acquisitions, this leads to blurring in reconstructed images, loss of axial resolution, and reduced accuracy in quantitative measurements of molecular structures. To achieve enhanced stability for super-resolution imaging, more advanced model-based controllers are needed, as they explicitly account for system dynamics and disturbances, enabling more accurate and robust drift compensation. For this, however, a model of the focal point dynamics is needed which in super-resolution microscopy is complicated, as the dynamics of the focal point are

highly influenced by physical changes to the optical setup due to temperature changes as a result of environmental temperature variability or heating and vibration from the stage due to electrical inputs.
One notable contributor to drift is the heating of optical components by the laser itself. In this thesis, we assume continuous-wave laser excitation. By preheating the optical parts for approximately 15 minutes before starting an experiment, the drift due to laser-induced heating stabilizes and can be neglected in the system identification. For setups in which the laser is not continuously applied, however, laser input variations could be explicitly included in the system identification procedure, as demonstrated in [15].

Subspace system identification methods, such as Numerical Algorithms for Subspace State Space System Identification (N4SID) [42], are effective in modeling complex dynamics within a linear time-invariant (Linear Time Invariant (LTI)) framework [15]. However, since the focal position dynamics are not autonomously stable and the measurement range is limited, applying random inputs during open-loop identification risks driving the system outside its valid operating range. To maintain the system within this range, a controller is necessary to correct the position, even during the generation of system identification data. In closed-loop settings, the feedback correlation between inputs and outputs complicates the separation of control actions from process noise [41]. Therefore, closed-loop system identification methods such as Predictor-Based Subspace IDentification optimal (PBSID_{opt}) can be applied to mitigate this issue.
When the system can be modeled, optimal control models such as Linear Quadratic Gaussian (LQG) can be implemented to compensate the drift, a similar approach for control in adaptive optics was previously performed in [22] by Caroline Kulcsár et al.

To maximize impact in the field of SRM, it is essential to identify the optimal combination of drift identification methods and subsequent control of focal point dynamics by considering the specific contexts in which SRM is applied. This MSc. Thesis serves as a Proof of Concept of a drift mitigation strategy that can be used by the largest group of SRM practitioners: biologists utilizing standard CPUs and commercial microscopes with limited capacity for hardware modification. To ensure the research findings are applicable to this group, the research objective is defined as follows:

"How can sample drift-induced resolution drop in SMLM be minimized using an actively controlled system that operates under typical SMLM constraints, enabling stable imaging in environments where computational resources are limited and modifications to the optical setup are not feasible?"

1-2 Organization

Chapter 2 reviews relevant work in the field of optics that forms the foundation for the method proposed in this thesis. Section 2-1 presents the current state of drift estimation techniques, while Section 2-2 explores how model-based control is applied in optical systems.

Chapter 3 highlights the original contributions of this thesis. The first part is structured as a scientific paper, detailing the developed method and presenting experimental results that demonstrate its significance. The second part serves as a supplementary document, providing additional experimental data and theoretical background supporting the proposed approach.

Finally, Chapter 4 offers a comprehensive summary of the thesis. It discusses the results in depth and outlines potential directions for future research aimed at advancing drift correction in super-resolution microscopy.

Chapter 2

Related Work

2-1 Drift estimation methods

Accurate drift estimation is critical for achieving high-resolution imaging in Single-Molecule Localization Microscopy (SMLM). Over the years, researchers have developed a variety of techniques to measure and correct sample drift during long acquisitions. These methods are commonly classified into three categories: *image reconstruction-based*, *beam-based*, and *fiducial marker-based* approaches. Each category presents trade-offs in terms of precision, real-time applicability, and hardware complexity.

2-1-1 Image Reconstruction-Based Drift Estimation

Image reconstruction-based methods estimate drift by analyzing the sequence of images or localization data. These approaches operate entirely in post-processing and do not require additional hardware. Three notable techniques are:

- **Redundant Cross-Correlation** estimates drift by maximizing the cross-correlation between overlapping image subsets. While computationally efficient, its precision is lower than other methods [23, 44].
- **Bayesian Sample Drift Inference** frames drift estimation as a Maximum A Posteriori problem and applies expectation-maximization to iteratively infer drift. It achieves high accuracy but can become slow for large datasets [12].
- **Drift at Minimum Entropy** estimates drift by minimizing the entropy of the final reconstructed image, assuming that minimal drift yields the sharpest image. It offers higher accuracy than Redundant Cross-Correlation and lower computational demand than Bayesian Sample Drift Inference [9].

- **Adaptive Intersection Maximization** estimates drift by maximizing the intersection of localization pairs across temporally distinct datasets. It enables the most precise spatial drift estimation out of the image reconstruction-based methods at sub-Ångström level, while being computationally efficient and usable with a CPU only [24].

These methods are ideal for systems where hardware modifications are not feasible. However, as they operate post-acquisition, they cannot support real-time drift correction, especially problematic for axial drift and 3D SMLM.

2-1-2 Beam-Based Drift Estimation

Beam-based methods allow real-time drift correction by analyzing laser light interactions with the sample. Representative techniques include:

- **Speckle pattern tracking** leverages the backscattered laser light from the sample to identify drift via cross-correlation with a pre-recorded z-stack. While effective, it requires a static sample and repeated removal of emission filters, limiting usability [6].
- **Nikon Perfect Focus** systems and their derivatives reflect a secondary laser off the sample plane onto a CCD or QPD sensor. Drift is inferred from beam displacement and compensated via feedback control [1].
- **Engineered Point Spread Function (PSF)s**, such as astigmatism or double-helix PSFs, induce z-dependent PSF deformation. By fitting these PSFs, 3D position can be extracted with high precision [21, 33, 43].

Despite enabling live compensation, all beam-based methods require significant optical modifications, additional lasers, lenses, sensors, or moving parts, posing challenges for integration with commercial microscope systems.

2-1-3 Fiducial Marker-Based Drift Estimation

Fiducial marker-based methods use fluorescent beads or gold Nano Particle (NP) attached to the sample substrate as stable reference points. During the last decade, it has been shown that these methods are the most viable approach, reaching sub-nanometer drift correction, as can be seen in Table 2-1. It is evident that most drift correction methods rely on gold NPs as fiducial markers and employ near-infrared illumination, either from a laser or LED, alongside a secondary Complementary Metal-Oxide-Semiconductor (CMOS) camera.

Publication	Fiducial Type	Drift Correction Precision lateral/axial (nm)	Control bandwidth	Modification Needed
P. Bon (2015) [4]	100nm Gold NPs	0.7/2.7	50Hz	transillumination 640nm laser + 2^{nd} CMOS
A. Balinovic (2019) [2]	200nm fluorescent beads	7.7 /-	33Hz	None
S. Coelho (2020) [10]	3μm Polystyrene beads	0.4/1.0	15Hz	transillumination of IR laser + 2^{nd} CMOS
R. Schmidt (2021) [36]	40nm Gold Nanorods	0.4/0.6	40Hz	IR laser + 2^{nd} CMOS
M. Weber (2021) [45]	40nm Gold Nanorods	<1/<1	80Hz/30Hz	IR LED + 2^{nd} CMOS
L. Massulo (2022) [27]	100nm Gold NPs	1.2/2	20Hz	IR LED + 2^{nd} CMOS + 3 BSs
S. Patil (2025) [30]	100nm Gold NPs	0.85/0.89	100Hz	Cylindrical lens + IR laser + 2^{nd} CMOS
X. Sun (2025) [39]	150nm Gold NPs	0.31/036	50Hz	IR laser + 2^{nd} CMOS

Table 2-1: Comparison of fiducial marker drift correction methods in SMLM.

The IR light is reflected by the gold NPs, and the secondary CMOS is dedicated to capturing only this reflected signal. This dual-camera configuration is essential because, in a single-camera setup, the intense reflected light from the NPs would saturate the sensor, thereby preventing the detection of the much weaker fluorescence signal from the sample. Consequently, most of hese approaches are not compatible with single-CMOS systems and require additional hardware for effective drift correction.

Single-CMOS approach

For one method fluorescent light emitted by the bead is used to determine the drift by A. Balinovic [2]. Although, as can be seen from the table, it only reaches a drift correction precision of 7.7 nm in lateral direction and has not shown results for the axial direction, this is a method that can be performed with a single camera. That is because the excitation laser light can be filtered and the emitted light by the beads is not saturating the camera. Resulting in a similar shaped PSF generated from reflection of gold NPs.

Estimating position from fiducial marker PSF

The fiducial markers are tracked across frames to estimate drift. Two primary approaches are:

- **Centroiding** estimates drift by comparing the center of mass (centroid) of two successive images of a particle. It is computationally simple and efficient but is sensitive to changes in particle shape or orientation between frames, resulting in low precision drift estimation. [5].

- **Gaussian fitting** determines the center of the fiducial PSF by fitting a 2D Gaussian using optimization techniques. This method is accurate but computationally intensive and benefits from GPU acceleration [25].
- **Phasor approach** uses the second Fourier components of the image to estimate the position of the fiducial marker. It achieves similar accuracy as Gaussian fitting but with over 100-fold speed improvement using only CPU resources [26].

  [19]

2-1-4 Conclusion

In summary, while image reconstruction and beam-based methods offer viable drift estimation strategies, they either lack real-time capabilities or require substantial optical modifications. In contrast, fiducial marker-based approaches provide a compelling balance between precision, real-time feedback, and ease of integration, especially when leveraging efficient tracking algorithms like the phasor method.

However, nearly all high-precision fiducial-based systems rely on a dedicated secondary CMOS camera to detect the reflected IR light from gold NPs, preventing interference with fluorescence imaging. This requirement increases system complexity, cost, and footprint, making these solutions less accessible for standard commercial microscope platforms.

By using the fluorescence of fiducial markers rather than their reflectance, combined with the phasor method, we obtain a drift estimation technique well-suited for commercial microscopes and standard CPUs. This approach strikes a balance between drift measurement precision, computational efficiency, and practical implementation, requiring only a single camera. As a result, phasor-based fluorescent fiducial marker tracking becomes the preferred method for SMLM setups where hardware modifications are not feasible, but sample adaptation is acceptable.

2-2 Model-Based Control in the Field of Optics

In parallel with the rise of drift estimation methods, the introduction of model-based control strategies in optical systems has shown significant promise for enhancing stability and precision. By leveraging mathematical models of system dynamics, model-based control enables predictive feedforward compensation of disturbances such as focus drift, offering advantages over traditional feedback methods. In the context of SMLM, combining a drift measurement approach that does not need a second camera with model-based control paves the way for real-time, hardware-independent and optimal drift correction.

2-2-1 System Identification

To enable the use of model-based controllers, a mathematical representation of the system dynamics is essential. In cases where the physics of the system are well understood, a first-principles model can often be derived directly. However, in many optical systems, especially those used in high-resolution microscopy such as SMLM, direct modeling becomes impractical due to unmodeled disturbances. These include unknown mechanical vibrations, nonlinearities introduced by temperature fluctuations, and electrical or sensor noise, all of which are often system-specific and difficult to characterize analytically.

In such scenarios, system identification becomes a crucial tool. System identification refers to the process of building mathematical models of dynamic systems based on observed input-output data. In the context of optics, this allows for capturing the behavior of components such as stages, actuators, lenses and feedback loops without requiring detailed physical insight.

A commonly used structure in system identification is the discrete-time Linear Time Invariant (LTI) state-space model:

$$\begin{aligned} \boldsymbol{x_{t+1}} &= A\boldsymbol{x_t} + B\boldsymbol{u_t} + w_t, \quad w_t \sim \mathcal{N}(0, Q), \\ \boldsymbol{y_t^m} &= C\boldsymbol{x_t} + D\boldsymbol{u_t} + v_t, \quad v_t \sim \mathcal{N}(0, R). \end{aligned} \tag{2-1}$$

where $\boldsymbol{x_t} \in \mathbb{R}^n$ is the state vector, $\boldsymbol{u_t} \in \mathbb{R}^m$ is the input (e.g., actuator signal), $\boldsymbol{y_t^m} \in \mathbb{R}^p$ is the measured output (e.g., bead position), and A, B, C, D are system matrices to be estimated. The terms w_k and v_k represent process and measurement noise, respectively.

In optical systems, system identification techniques are increasingly used to model complex interactions that are difficult to describe analytically. For instance, Haber et al. [16] demonstrate the application of subspace system identification to estimate low-order state-space models of transient Structural-Thermal-Optical-Performance (STOP) dynamics in reflective optics. In their work, simulated wavefront aberration data, originating from heat-induced mechanical deformations, is used to identify a reduced-order model of a Newtonian telescope system. The identification is performed using a subspace method, which estimates the system matrices from time series of input (laser power) and output (Zernike coefficients) data. This approach enables accurate modeling of the coupled thermal-structural-optical dynamics, resulting in compact models suitable for real-time control and prediction of thermally-induced wavefront aberrations. Such techniques highlight the potential of data-driven modeling for enabling model-based control strategies in advanced optical setups.

2-2-2 Open-Loop and Closed-Loop System Identification

Traditional subspace identification methods typically assume that the plant under investigation is identified with open-loop data. However, this assumption does not hold for systems that must be controlled to remain stable or need to be controlled to a certain operating range. Using closed-loop data, however, introduces a complication: the control input $\boldsymbol{u_k}$ at time step k becomes correlated with the measurement noise v_j at past time step j, violating the standard system identification requirement that,

$$\mathbb{E}\{\boldsymbol{u_k} v_j\} = 0 \text{ for } j < k, \tag{2-2}$$

which is true for open-loop systems. Hereby, when using a subspace identification method such as Numerical Algorithms for Subspace State Space System Identification (N4SID) [42], the measurement noise is not decoupled from the inputs during subspace matrix estimation. The resulting correlation between input and noise under closed-loop conditions introduces bias in the identified system matrices.

To address this limitation, Predictor-Based Subspace IDentification optimal (PBSID$_{opt}$) [8] can be employed. PBSID$_{\mathrm{opt}}$ performs a two-step estimation that explicitly handles feedback-induced input–noise correlation.

First, the state-space equations in Eq. 2-1 is rewritten in data equation form as:

$$\boldsymbol{Y}_{p,N_p} = \begin{bmatrix} C & D \end{bmatrix} \begin{bmatrix} \hat{\boldsymbol{X}}_{p,N_p} \\ \boldsymbol{U}_{p,N_p-1} \end{bmatrix} + \boldsymbol{E}_{p,N_p}, \tag{2-3}$$

$$\boldsymbol{X}_{p+1,N_p-1} = \begin{bmatrix} A & B & L \end{bmatrix} \begin{bmatrix} \hat{\boldsymbol{X}}_{p,N_p-1} \\ \boldsymbol{U}_{p,N_p-1} \\ \boldsymbol{E}_{p,N_p-1} \end{bmatrix}. \tag{2-4}$$

Here the notation for the set $\boldsymbol{Y}_{p,N_p}$ is used to denote a block-row matrix:

$$\boldsymbol{Y}_{p,N_p} = \begin{bmatrix} \boldsymbol{y}_i & \boldsymbol{y}_{i+1} & \dots & \boldsymbol{y}_{i+N-p-1} \end{bmatrix}, \tag{2-5}$$

where $N_p = N - p$.

Equation 2-3 is first solved via least squares to estimate the output matrix C and the innovation sequence $\boldsymbol{E}_{p,N_p}$, which captures the residual prediction error. This innovation is then treated as a known signal and substituted into Eq. 2-4, which is again solved using least squares to estimate the matrices A, B, and L.

By modeling the system in predictor form and isolating the innovations, PBSID$_{opt}$ avoids the input-noise correlation that biases standard subspace methods like N4SID. A full derivation of these data equations and estimation steps is provided in Appendix A.

2-2-3 Model-Based Control

Model-based control strategies rely on an internal model of system dynamics to compute control actions in a predictive, often optimal manner. In contrast to traditional controllers such as proportional-integral-derivative (PID), which rely solely on error feedback, model-based approaches incorporate knowledge of system behavior and disturbance characteristics to anticipate future system states and compensate accordingly. This is particularly useful in optical systems.

A prominent example of model-based control in optics is provided by Kulcsár et al. [22], who address residual phase variance minimization in adaptive optics using a Linear Quadratic Gaussian (LQG) control framework. Their approach separates the control problem into two parts: an optimal control component, solved via Linear Quadratic (LQ) control, and an optimal state estimation component, solved using a Kalman filter. The resulting LQG controller minimizes a quadratic cost function of the form

$$J(u) = \lim_{n \to \infty} \frac{1}{n} \sum_{k=1}^{n} \|\phi_k^{\mathrm{res}}\|^2, \tag{2-6}$$

where ϕ_k^{res} denotes the real residual phase error at time step k. This cost function quantifies image degradation and is minimized by adjusting the control inputs u_k based on noisy measurements from a wavefront sensor. The optimal control law takes the form

$$u_k = K\hat{x}_{k+1|k}. \tag{2-7}$$

where $\hat{x}_{k+1|k}$ is the predicted system state, which is obtained from a Kalman filter in which the lowest variance estimate of the residual phase, $\hat{\phi}^{\text{res}}_{k+1}$ is encapsulated. Further, K is a feedback gain matrix derived from the solution to the LQ problem. The Kalman filter updates the state estimate by combining the model prediction with new measurement data, thereby reducing the impact of noise and unmodeled dynamics.

This framework provides a powerful basis for implementing model-based control in SMLM systems, enabling precise drift correction by explicitly modeling the thermal or mechanical disturbances affecting the imaging process.

Chapter 3

Manuscript

Hardware Modification Free Active 3D-Drift Correction in Single-Molecule Localization Microscopy (SMLM)

K.E. BLOKHUIS[1], L. COOLS[1], D. KROMM [1], R.P. TAS[2], C.S. SMITH[1,*]

[1] *Delft Center for Systems and Control, Delft University of Technology, Delft, the Netherlands.*
[2] *Delft University of Technology, Delft, the Netherlands.*
[*]

Abstract: Single-molecule localization microscopy (SMLM) enables nanometer-scale imaging but is highly sensitive to sample drift. We present an active 3D drift correction method using only fiducial markers, requiring no hardware modifications. Fluorescent light from fiducials is extracted directly from the main imaging camera during acquisition. The computationally efficient Phasor approach estimates 3D bead positions [1], making correction limited mainly by camera frame rate (e.g., >22 Hz at 25 fps). Experiments demonstrate closed-loop stability with 1.1 nm lateral and 2.9 nm axial precision, highlighting the potential of our hardware modification free, real-time drift correction approach for high-resolution SMLM.

1. Introduction

Super-resolution microscopy (SRM) has enabled researchers to achieve spatial resolutions far beyond the diffraction limit of conventional optical microscopy, which is approximately half the wavelength of visible light (≈200 nm). Over the past three decades, various techniques have been developed to serve the diverse needs of biologists and microscopists [2]. The best-known SRM methods are commonly categorized into three groups: STimulated Emission Depletion (STED) [3], Structured Illumination Microscopy (SIM) [4], and Single-Molecule Localization Microscopy (SMLM) [5–8].

Unlike STED and SIM, SMLM typically requires long acquisition times, often lasting several minutes, during which thousands of raw images are collected to reconstruct a final super-resolved image. During this period, it is critical that the sample remains at a stable focal position relative to the objective lens. Even small amounts of three-dimensional (3D) drift can degrade the achievable resolution. This drift is primarily caused by environmental instabilities such as temperature fluctuations, mechanical vibrations, and thermal effects within the optical path, e.g. laser-induced heating of optical components or thermal expansion of the stage due to increased environment temperature.

To mitigate the effect of drift, several strategies for drift measurement have been proposed, which can be broadly classified into three categories: image reconstruction-based, beam-based, and fiducial marker-based approaches. Image reconstruction-based methods estimate drift from the single-molecule localization data itself, for example using image cross-correlation techniques [9]. Beam-based methods actively track the sample's position using a laser reflected from the coverslip surface. For example, [10] employ an engineered Point Spread Function (PSF) to correlate live back-reflected images from the laser with a reference z-stack. Fiducial marker-based methods use fluorescent beads or gold nanoparticles as static reference points within the sample [11,12]. These markers can be tracked over time, and active control algorithms can dynamically compensate for measured drift in real time. All three methods have limitations. Image cross-correlation is restricted to post-processing and therefore cannot provide real-time correction, which results in unresolved axial drift resolution loss. Beam-based approaches typically require modifications to the optical setup, including the use of a cylindrical lens to obtain an engineered PSF and an additional camera or a CCD sensor as in Nikon's Perfect Focus System (PFS) [13] to read the reflection. Similarly, most fiducial marker-based methods rely on back-reflected IR light from gold nanoparticles, which also necessitates a separate camera.

Most existing control implementations rely on relatively simple proportional–integral–derivative (PID) controllers [11]. However, to enable optimal control of drift, it is essential to apply Kalman filtering to suppress noise in the measurements and perform model-based control to preemptively compensate for drift [14]. This requires a mathematical model of the system dynamics, which can be obtained through system identification techniques. Subspace-based identification methods, such as N4SID [15] and its closed-loop system identification counterpart PBSID$_{opt}$ [16, 17], have shown to be well suited for estimating the linear time-invariant (LTI) models needed for optimal filtering and control [18].

In this paper, we present a hardware modification free, fiducial marker-based 3D drift correction system for SMLM. Our method relies solely on the main acquisition camera to track fluorescent fiducial markers, avoiding the need for additional hardware or optical paths, and making it easily implementable in both commercial and custom-built microscopes, as only fiducial markers need to be bought and added to the sample. To overcome the lower signal-to-noise ratio (SNR) of fluorescent fiducials compared to infrared-illuminated gold nanoparticles, we employ optimal Kalman filtering to reduce measurement noise and enhance localization precision. By leveraging the computationally efficient Phasor approach for 3D position estimation [1], our system operates at rates limited only by the camera's frame rate without the use of a GPU, achieving drift correction with a precision of 0.6 nm in lateral and 2.4 nm in axial directions at >20 Hz rates. In addition, we implement a smart illumination strategy using periodic z-stacking, to limit falsely perceived drift over long acquisitions.

2. Methods

2.1. Experimental Setup

A schematic of the optical setup is illustrated in Fig. 1.(a). The optical setup is a TIRF (Total Internal Reflection Fluorescence) microscope, which exploits evanescent wave excitation at the glass-water interface to selectively illuminate fluorophores within 100-200 nm of the coverslip, reducing background fluorescence. Two lasers, a 405 nm and a 640 nm laser are combined using a dichroic mirror and focused onto the coverslip. These lasers excite the fiducial markers, and the fluorophores from the sample respectively. The light returning from the cover slip is a cumulation of the fluorescent light from the activated single-molecules in the sample and the fluorescent beads, as shown in Fig. 1.(b). As presented in Table 1, frequently, setups with fiducial marker-based drift correction use a dichroic mirror to split light coming from the markers and sample and capture them separately on two cameras. In our setup, no additional dichroic mirror or secondary camera is used; instead, all fluorescence emission is collected on a single detector. As a result, potential residual drift commonly observed in dual-camera configurations, caused by thermally induced mechanical deformations after the optical path is split by a dichroic mirror, is inherently avoided. After analysing each recorded image, the piezo-electric stage is controlled to account for the drift. A detailed illustration of the optical setup can be found in Fig. S1.

2.2. Theory for drift estimation

Estimating the lateral sample drift is achieved by analysing the 2D Discrete Fourier transform of the current image $F(x, y)$, to the desired image $G(x, y)$, specifically comparing the second Fourier coefficients' phasor angles of the bead's PSF at the desired focal point, $(\phi_{b,0,x}, \phi_{b,0,y})$ and the current focal point $(\phi_{b,f,x}, \phi_{b,f,y})$, as presented in [1] such that,

$$\Delta x_{b,f} = \frac{px(\phi_{b,0,x} - \phi_{b,f,x})}{2\pi}, \tag{1}$$

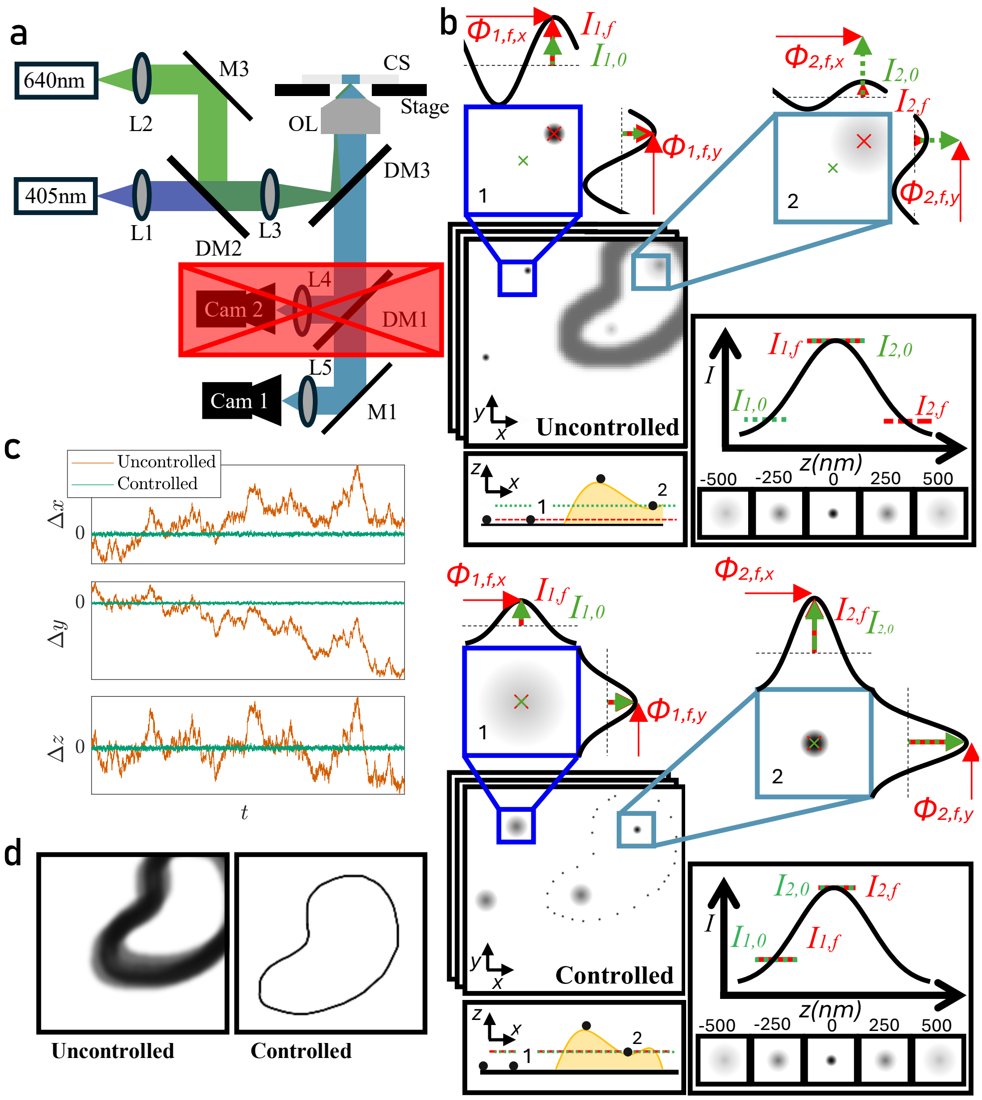

Fig. 1. (a) Schematic of the optical setup. M: mirror, DM: dichroic mirror, OL: objective lens, L: lens, CS: coverslip, F: filter. DM1, L4 and Cam 2 are not included in the experimental setup but are commonly used in other sub-nanometer drift measurement methods. (b) Schematic of the position estimation process for the focus point in 2 scenarios: Uncontrolled stage (top), Controlled stage (bottom). Zoomed-in regions show bead 1 (on the coverslip) and bead 2 (on top of the sample). The bead's phasor angles $\phi_{b,f,x}$, $\phi_{b,f,xy}$ and magnitude $I_{b,f}$, in the current frame are shown in red; the green arrow indicates the desired phasor magnitude, $I_{b,0}$. The red and green cross show the current and desired lateral position of the bead, respectively. (As the intensity profile is symmetrical in both x and y, the phasor magnitude is only displayed once per bead.) (c) 3D focus drift over time. (d) Final SMLM reconstruction.

where px represents the pixel size (nm). The lateral displacement between the two for bead, b, at frame, f, is denoted as $d_{b,f} = (\Delta x_{b,f}, \Delta y_{b,f})$.

By only comparing two Fourier coefficients of the current frame, to two Fourier coefficients of the desired frame, this approach is computationally efficient and requires only a CPU, in comparison to [19], where GPU optimization is used to perform a full cross-correlation of the Fourier transformations, to reach an acceptable control bandwidth.

For axial drift estimation, a z-stack is captured prior to the acquisition sequence. The second Fourier coefficients' amplitude of the bead's PSF, I_b, is determined at each z-position. While the bead's PSF is not altered by e.g. an astigmatic lens, it can be represented as a symmetric 2D-Gaussian. Therefore, as the beads go in and out of focus, both the x and y phasors' amplitude follow an identical Gaussian fit. This fit is used during the acquisition sequence. First the z-position of the desired focal point is determined. In the following frames, the desired position is compared with the current frame's z-position, which is estimated using the current phasor magnitude and precalculated Gaussian fit. Completing the drift vector to $d_{b,f} = (\Delta x_{b,f}, \Delta y_{b,f}, \Delta z_{b,f})$. The average over all N beads is taken as the final measurement, $\bar{d}_f = (\overline{\Delta x_f}, \overline{\Delta y_f}, \overline{\Delta z_f})$.

Table 1. Comparison of fiducial marker-based drift correction methods.

Publication	**Fiducial Type**	**Drift Correction Precision lateral/axial (nm)**	**Control bandwidth**	**Modification Needed**
P. Bon (2015) [20]	100 nm Gold NPs	0.7/2.7	50 Hz	Transillumination 640 nm laser + 2nd CMOS
A. Balinovic (2019) [21]	200 nm fluorescent beads	7.7 /-	33 Hz	None
S. Coelho (2020) [11]	3μm Polystyrene beads	0.4/1.0	15 Hz	Transillumination of IR laser + 2nd CMOS
R. Schmidt (2021) [22]	40 nm Gold Nanorods	0.4/0.6	40 Hz	IR laser + 2nd CMOS
M. Weber (2021) [23]	40 nm Gold Nanorods	<1/<1	80 Hz/30 Hz	IR LED + 2nd CMOS
L. Massulo (2022) [24]	100 nm Gold NPs	1.2/2	20 Hz	IR LED + 2nd CMOS + 3 BSs
S. Patil (2025) [25]	100 nm Gold NPs	0.85/0.89	100 Hz	Cylindrical lens + IR laser + 2nd CMOS
X. Sun (2025) [19]	150 nm Gold NPs	0.31/036	50 Hz	IR laser + 2nd CMOS

Fig. 1.(b) shows the phasor approach drift estimation of two beads in two scenarios; actively controlled and uncontrolled. The first bead lays on top of the coverslip, the second bead is on top of the sample. The first frame taken in the acquisition cycle is the manually determined in-focus frame and therefore the desired frame. With the uncontrolled setup, lateral drift results in an equal lateral drift of the beads and change in phasor angles $\phi_{b,f,x}$ and $\phi_{b,f,y}$. Due to a shift in the axial direction, the phasor magnitudes moved away from their initial magnitude as well. In the controlled scenario, the phasor angle and magnitude are actively estimated and compared to the desired angles and magnitudes. Interaction of these measurements with the stage then compensates for any drift estimated with the phasor approach such that phasor angle and magnitude remain at the desired values.

It is important to note that, in the absence of prior knowledge of the bead positions, the magnitude of the PSF phasor alone cannot distinguish between positive and negative axial offsets. This is due to the symmetry of the fit with respect to the focal plane (see Supplementary Fig. S2). However, after we perform the z-stack, we know each bead's z-position based on the peak of the Gaussian fit, such that when the desired focal position is set, it is possible to determine whether it is positioned above or below each bead. Therefore, only the corresponding half of the phasor magnitude curve can be used for position estimation.

Since the sensitivity of axial position estimation is proportional to the derivative of the intensity with respect to the axial position, dI/dz, the operational axial range of each fiducial bead, denoted $z_{or,b}$, is manually selected based on the axial profile of the Gaussian fit. For $1\mu m$ fiducial beads, this operational range typically spans from approximately 400 nm below to 100 nm below the focal plane of the bead, and from 100 nm to 400 nm above the focal plane of the bead. The ±100 nm region surrounding the focal plane of the bead is excluded due to the ambiguity in determining whether the focal plane lies above or below the bead, as well as the reduced sensitivity of the intensity profile in this region, where dI/dz approaches zero at the point of maximum phasor magnitude. This is accompanied by a trade-off with bead size: larger beads exhibit a wider operating range due to their broader axial response, but they also occupy more space in the imaging frame, which can reduce the number of usable fiducials or interfere with the sample. An alternative strategy to overcome the limited axial range of individual fiducials is to embed beads at different axial heights within a transparent medium such as agarose gel, allowing their operational ranges to overlap. This effectively extends the total usable axial detection range for drift correction or localization.

2.3. System identification

The dynamics of the focus point can be described using a linear discrete-time state-space model:

$$\boldsymbol{x_{k+1}} = A\boldsymbol{x_k} + B\boldsymbol{u_k} + w_k, \quad w_k \sim \mathcal{N}(0, Q), \tag{2}$$

$$\boldsymbol{y_k} = C\boldsymbol{x_k} + D\boldsymbol{u_k} + v_k, \quad v_k \sim \mathcal{N}(0, R), \tag{3}$$

where $\boldsymbol{x_k} \in \mathbb{R}^n$ is the state vector, $\boldsymbol{u_k} \in \mathbb{R}^m$ is the input (e.g., stage input), $\boldsymbol{y_k} \in \mathbb{R}^p$ is the measured output (e.g., focus position), and A, B, C, D are system matrices to be estimated. The terms w_k and v_k represent the process and measurement noise, respectively, with Q and R denoting their corresponding covariance matrices, i.e., $\mathbb{E}[w_k w_k^\top] = Q$ and $\mathbb{E}[v_k v_k^\top] = R$.

Assuming that the drift follows a purely Gaussian process and that the piezoelectric stage introduces motion strictly proportional to the applied control inputs, without exerting a direct effect on the measurements, the system matrices can be reduced. Specifically, the state-space representation simplifies to $A = B = C = I_3$ and $D = 0$. We refer to this simplified structure as the *Identity model*. While this model serves as a useful baseline, it does not capture potentially significant higher-order dynamics present in the experimental system. Therefore, to obtain a more accurate representation of the underlying system behavior, we employed data-driven system identification techniques. In particular, the Numerical algorithms for Subspace State Space System Identification (N4SID) method [15] and the optimal Predictor-Based Subspace Identification approach (PBSID$_{\text{opt}}$) [17] were used to estimate the state-space matrices from observed input-output data.

Identifying such a model is critical for optimal control strategies, as it provides a structured representation of the system's dynamics in terms of states, inputs, and outputs. In particular, expressing the system in a state-space form enables the use of linear control and estimation techniques, such as the Kalman filter and Linear Quadratic Regulator (LQR). Even for systems with nonlinear behavior, linear state-space models around an operating point allow for effective local control, in this case around our desired focus point. Moreover, having an explicit model of the dynamics allows for one-step-ahead predictions of the system's evolution, enabling anticipatory feedback that can preemptively counteract disturbances. A detailed description of the system identification experiments is provided in Supplementary Section 3, which includes the methodology for model order and hyperparameter selection. This section also presents a comparison between open-loop and closed-loop identification approaches, as well as a validation-based evaluation of the identified model against a simplified identity model.

2.4. Counteracting Bead Emission Instability Effects

A fundamental limitation of using fluorescent fiducial markers for axial drift estimation is the photo instability of their fluorescence emission. Since the axial position is inferred from the phasor magnitude, which is proportional to the fluorescence intensity, photo instability can lead to systematic errors. In particular, a reduction in phasor magnitude may be falsely interpreted as axial drift, prompting the system to apply incorrect compensatory stage movements.

During experiments we have observed two causes for photo instability, first: under constant excitation conditions, the normalized fluorescence intensity of the markers decays exponentially over time, and can be modeled as: $F(t) = e^{-t\tau}$, where τ is the bleaching rate constant. Increasing the excitation power leads to an increase in τ, thereby accelerating photobleaching [26]. It is therefore crucial to minimize excitation power to preserve photostability, as previously recommended in [21]. In our experiments, we found that maintaining the excitation intensity at approximately 35 W/cm^2 ensured both sufficient signal strength and stable drift estimation when using 1μm Thermo Fisher Tetra speck beads.

Despite low-power excitation, residual photobleaching persists. To correct for its impact on phasor magnitude, we employ autonomous intermittent z-stacking to recalibrate phasor intensity curves over time. We found that updating the reference z-stacks every 1000 frames effectively mitigated bleaching-induced errors in drift estimation (see Supplementary Section 5 for additional details).

However, when acquiring multiple z-stacks in rapid succession, we occasionally observed unexpected increases in the phasor magnitude. Several factors may contribute to this phenomenon. First, laser power instability is a likely cause; fluctuations were particularly noticeable at output powers below 5% of the nominal value, where laser regulation is less precise. Second, variations in optical throughput due to thermal expansion of optical components may alter system efficiency over time. Third, although a pi shaper is used to transform the excitation beam from a Gaussian to a top-hat profile, residual non-uniformities across the field of view (FOV) may still be present, potentially leading to localized intensity fluctuations.

3. Results

3.1. System Identification

To identify the system dynamics, we analyzed the mean position of eight 1 µm Thermo Fisher TetraSpeck fluorescent beads, excited with a 488 nm laser at 35 W/cm^2 and recorded using a camera exposure time of 35 ms. A schematic overview of the system identification workflow is provided in Supplementary Section 5. The measurement noise standard deviations were estimated to be $\sigma_x^m = 0.53$ nm, $\sigma_y^m = 0.81$ nm, and $\sigma_z^m = 2.2$ nm in the respective spatial directions.

Among the models tested, the identity model yielded the lowest Root Mean Squared Error (RMSE) between the measured and estimated displacements: $\text{RMSE}_{\Delta x} = 0.62$ nm, $\text{RMSE}_{\Delta y} = 1.1$ nm, and $\text{RMSE}_{\Delta z} = 2.8$ nm. Although the identified models captured the dominant drift dynamics with relatively high accuracy in all three spatial directions. No improvement in RMSE was observed when increasing the model order, suggesting that the drift dynamics do not exhibit significant higher-order behavior. Additional quantitative results are presented in Supplementary Section 3.

3.2. Drift Correction Performance

The proposed hardware modification free drift correction method demonstrated stabilization performance at the nanometer scale. To validate the correction performance, the same optical setup and experimental conditions were used as in the system identification procedure.

Fig. 2(a) shows the 3D mean bead displacements over time, including their desired position at $\bar{\Delta} = 0$. It is shown that the active control loop is able to actively stabilize the focus point around

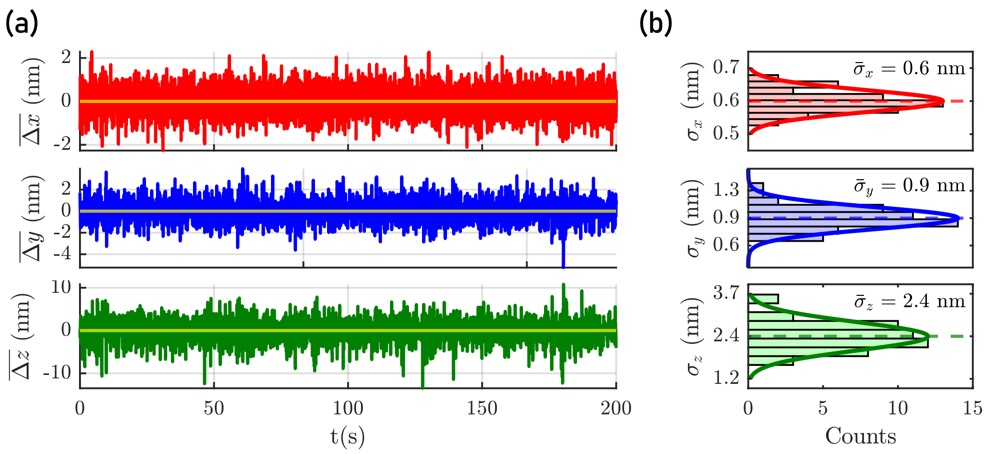

Fig. 2. (a) Mean displacements $\Delta x, y, z$ of the focus point from the reference position, estimated using fiducial beads. (b) Estimated probability density functions of the standard deviations of 3D sample drift from (a), computed over 5-second segments. Solid lines show Gaussian fits to the histograms; dashed lines indicate the corresponding distribution means.

the desired point.

In Fig. 2(b), a histogram of the standard deviation of the bead position measurements, calculated over a sliding window of 5 seconds, is shown alongside a fitted Gaussian distribution. The mean standard deviations over the full duration of the experiment were found to be $\bar{\sigma}_x = 0.6$ nm, $\bar{\sigma}_y = 0.9$ nm, and $\bar{\sigma}_z = 2.4$ nm in the respective spatial directions. These values closely match the estimated measurement noise levels obtained during system identification, indicating that the closed-loop drift correction approaches the theoretical lower bound imposed by the measurement noise. This suggests that the residual motion is dominated by the stochastic measurement process rather than uncorrected drift. Counteracting bead emission instability was reached using the proposed intermittent z-stacking protocol. It results in acquisition pauses of only 6.3 seconds during each z-stack, yielding an average of falsely perceived drift of 3.2 nm.

3.3. SMLM imaging of C3T3 cells

To evaluate the performance of our system during practical imaging of biological samples, an SMLM experiment was conducted using our real-time 3D drift correction method. Peptide-based PAINT was performed in fixed MC3T3 cells using Atto643-conjugated purified lifeAct that transiently bound to filamentous actin for single-molecule reconstructions. LifeAct-Atto643 was diluted 1:2.000.000 from stock solution so that single binding and unbinding events could be observed. Fiducial markers consisting of 0.22 μm LightYellow Spherotech beads were deposited onto the coverslip for active drift correction. A 642 nm laser was used for sample excitation and a 405 nm laser was used for bead excitation, imaging was performed using an excitation power density of approximately 35 W/cm^2 for sample excitation and 0.650 kW/cm^2 for bead excitation. The camera was operated with an exposure time of 35 ms and an effective pixel size of 108.33 nm in the sample plane. A total of 30,000 frames were recorded during the experiment. The resulting reconstruction is found in Figure 3(a), zooming in at one of the 0.22 μm Spherotech Light Yellow beads used for drift corrections in Figure 3(b) shows that its reconstruction forms a 2D Gaussian as highlighted in the intensity plot Figure3(c) indicating that most drift is compensated for.

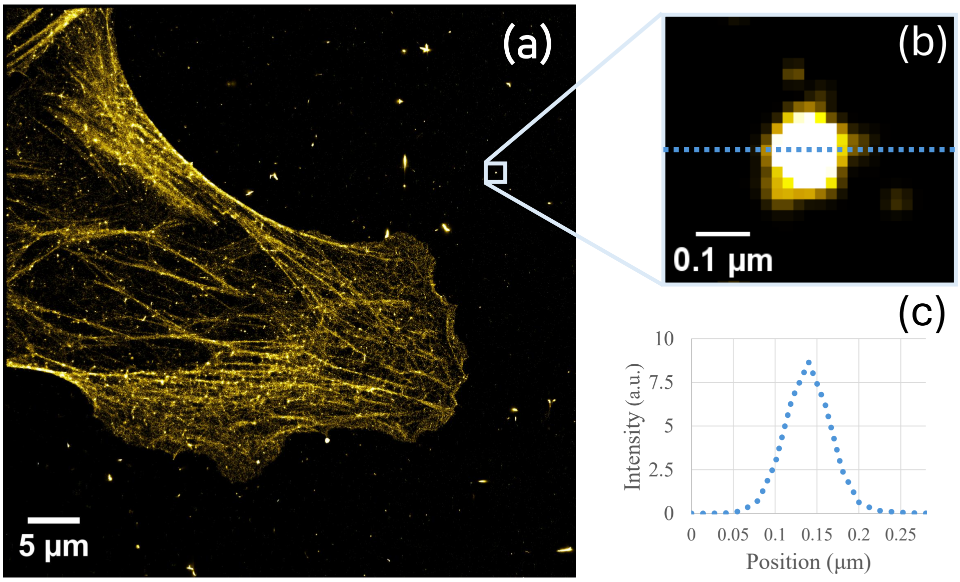

Fig. 3. Reconstructed image of fixed MC3T3 cells labeled with Atto643-conjugated purified lifeAct and using 0.22μm Spherotech Light Yellow beads for drift correction. (a) SMLM image with active drift correction. (b) Zoomed region showing the reconstruction of one of the fluorescent beads. (c) Intensity plot along the blue dotted line in (b), showing symmetrical intensity distribution of the fluorescent bead.

4. Discussion and conclusions

We have designed a hardware modification free active drift correction system that reaches high precision drift correction, relying only on fluorescent fiducial markers. Our method approaches the performance of many modification based drift correction systems, making it a viable option for commercial and non-commercial optical setups. With experimental validation we show sub-1 nm lateral and sub-3 nm axial drift correction. By using the computationally efficient phasor approach for measuring the drift, the control bandwidth is only limited by the camera's fps during acquisition, without the use of a GPU.

As there is no physical separation between the single-molecules reaching the acquisition camera and the fiducial markers' fluorescence reaching the drift correction camera, the implementation of a second camera is unnecessary. Consequently, this design inherently avoids the issue of residual drift, which is frequently neglected in other drift correction methodologies.

However, in contrast to reflectance-based approaches, our fluorescence-based method is susceptible to photo instability of the fluorescent beads. This photo instability induces changes in the phasor magnitude, which may be falsely interpreted as drift. To mitigate this limitation, we propose two strategies. First, we employ low-power excitation to minimize the rate of photobleaching. Second, we implement autonomous intermittent z-stacking at intervals of every 1000 frames to compensate for residual bleaching effects. While this approach mitigates the effects of bead photobleaching during acquisition, it also introduces limitations to the drift correction strategy. In particular, the reliance on intermittent z-stacking precludes continuous correction and results in a mean residual drift of 3.3 nm. A more advanced alternative would involve explicitly modeling the photobleaching process by incorporating the bleaching constant τ into the dynamical system following its identification. This would enable a continuous correction scheme that compensates for the gradual decay in fluorescence emission over time.

System identification methods such as N4SID and PBSID$_{\mathrm{opt}}$ did not result in improved performance compared to the Identity model, which assumes drift dynamics behave as Brownian motion. This suggests that, under the current measurement conditions, the drift is well-approximated by a random walk. However, the use of modified approaches with lower measurement noise could enable the identification of higher-order system dynamics. In this work, we have presented a structured framework for system identification, which may facilitate more accurate modeling and further improvements in drift correction performance in future implementations.

Disclosures. The authors declare no conflicts of interest

Supplemental document. See Supplement 1 for supporting content.

References

1. K. J. A. Martens, A. N. Bader, S. Baas, *et al.*, "Phasor based single-molecule localization microscopy in 3D (pSMLM-3D): An algorithm for MHz localization rates using standard CPUs," The J. Chem. Phys. **148**, 123311 (2017).
2. L. Schermelleh, A. Ferrand, T. Huser, *et al.*, "Super-resolution microscopy demystified," Nat. cell biology **21**, 72–84 (2019).
3. G. Donnert, J. Keller, R. Medda, *et al.*, "Macromolecular-scale resolution in biological fluorescence microscopy," Proc. National Acad. Sci. **103**, 11440–11445 (2006).
4. M. G. Gustafsson, "Surpassing the lateral resolution limit by a factor of two using structured illumination microscopy," J. microscopy **198**, 82–87 (2000).
5. E. Betzig, G. H. Patterson, R. Sougrat, *et al.*, "Imaging intracellular fluorescent proteins at nanometer resolution," science **313**, 1642–1645 (2006).
6. S. T. Hess, T. P. Girirajan, and M. D. Mason, "Ultra-high resolution imaging by fluorescence photoactivation localization microscopy," Biophys. journal **91**, 4258–4272 (2006).
7. M. J. Rust, M. Bates, and X. Zhuang, "Sub-diffraction-limit imaging by stochastic optical reconstruction microscopy (storm)," Nat. methods **3**, 793–796 (2006).
8. M. Heilemann, S. Van De Linde, M. Schüttpelz, *et al.*, "Subdiffraction-resolution fluorescence imaging with conventional fluorescent probes," Angewandte Chemie-International Ed. **47** (2008).
9. Y. Wang, J. Schnitzbauer, Z. Hu, *et al.*, "Localization events-based sample drift correction for localization microscopy with redundant cross-correlation algorithm," Opt. Express **22**, 15982–15991 (2014).
10. A. Rahmani, T. Cox, A. T. A. Achary, and A. Ponjavic, "Astigmatism-based focus stabilisation with universal objective lens compatibility, extended operating range and nanometre precision," bioRxiv (2024).
11. S. Coelho, J. Baek, M. S. Graus, *et al.*, "Ultraprecise single-molecule localization microscopy enables in situ distance measurements in intact cells," Sci. Adv. **6** (2020).
12. H. Ma, J. Xu, J. Jin, *et al.*, "A simple marker-assisted 3d nanometer drift correction method for superresolution microscopy," Biophys. J. **112**, 2196–2208 (2017).
13. "The nikon perfect focus system (pfs)," https://www.microscopyu.com/tutorials/the-nikon-perfect-focus-system-pfs (n.d.). Accessed: 2025-07-29.
14. C. Kulcsár, H.-F. Raynaud, C. Petit, *et al.*, "Optimal control, observers and integrators in adaptive optics," Opt. express **14**, 7464–7476 (2006).
15. P. Van Overschee and B. De Moor, "N4sid: Subspace algorithms for the identification of combined deterministic-stochastic systems," Automatica **30**, 75–93 (1994).
16. A. Chiuso, R. Muradore, and E. Fedrigo, "Adaptive optics systems: A challenge for closed loop subspace identifcation," in *2007 American Control Conference,* (IEEE, 2007), pp. 2949–2954.
17. A. Chiuso, "On the relation between cca and predictor-based subspace identification," IEEE Trans. on Autom. Control. **52**, 1795–1812 (2007).
18. A. Haber, "Subspace identification of temperature dynamics," arXiv preprint arXiv:1908.02379 (2019).
19. X. Sun, Z. Zhan, C. He, *et al.*, "Nanodriftguard: Open-source isotropic ångström-scale active stabilization for super-resolution microscopy," Opt. Lasers Eng. **190**, 108957 (2025).
20. P. Bon, N. Bourg, S. Lécart, *et al.*, "Three-dimensional nanometre localization of nanoparticles to enhance super-resolution microscopy," Nat. Commun. **6** (2015).
21. A. Balinovic, D. Albrecht, and U. Endesfelder, "Spectrally red-shifted fluorescent fiducial markers for optimal drift correction in localization microscopy," J. Phys. D: Appl. Phys. **52**, 204002 (2019).
22. R. Schmidt, T. Weihs, C. A. Wurm, *et al.*, "Minflux nanometer-scale 3d imaging and microsecond-range tracking on a common fluorescence microscope," Nat. Commun. **12** (2021).
23. M. Weber, M. Leutenegger, S. Stoldt, *et al.*, "Minsted fluorescence localization and nanoscopy," Nat. photonics **15**, 361–366 (2021).
24. L. A. Masullo, A. M. Szalai, L. F. Lopez, *et al.*, "An alternative to minflux that enables nanometer resolution in a confocal microscope," Light. Sci. & Appl. **11**, 199 (2022).

Hardware Modification Free Active 3D-Drift Correction in Single-Molecule Localization Microscopy (SMLM): supplemental document

1. OPTICAL SETUP

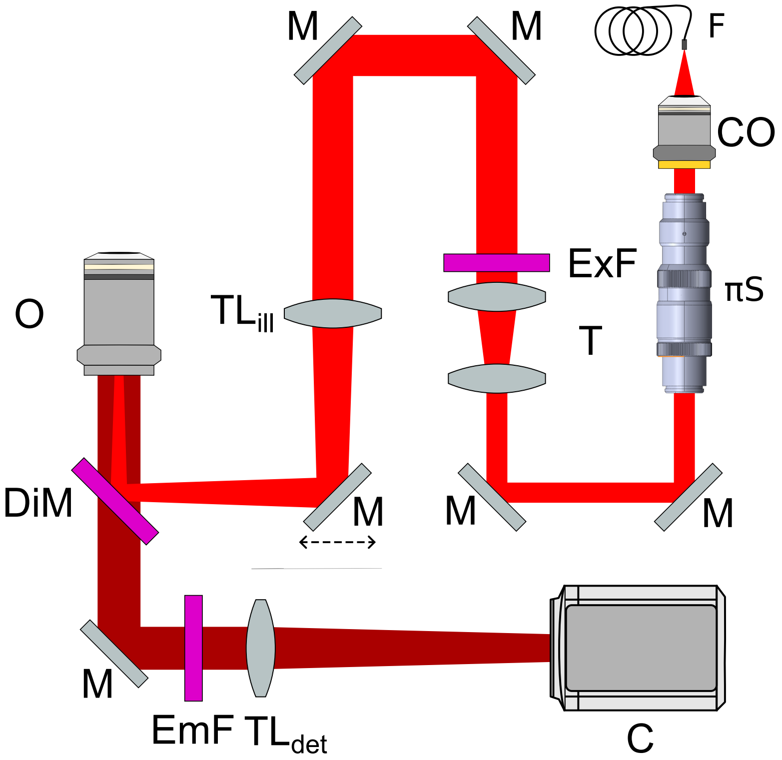

Fig. S1. Detailed schematic of TIRF microscope used for experiments. List of components in Table S1.

Table S1. Component Table

Component	Abbr.	Function	Parts Description / Name(s)	Vendor / Link	Qty
Optic Fibre	F	Guides light from laser combiner to microscope; "cleans up" laser modes	Polarization maintaining optic fibre, custom patch cable (PM-S405-XP, 3m, dual SMA connectors)	Thorlabs (PM-S405-XP)	1
Collimator	Co	Collimates laser beam to 6 mm	f = 35 mm, Ø1" Achromatic Doublet (AC254-035-A), f = 75 mm, Ø1" Achromatic Doublet (AC254-075-A)	Thorlabs (AC254-035-A,AC254-075-A)	1
Pi-Shaper	πS	Creates top-hat beam profile; input beam diameter critical	VIS Flat Top Beam Shaper (πShaper 6_6 Series, #12-644)	Edmund Optics (πShaper 6_6 Series)	1
Mirror (1 & 2)	M	Reflects beam; alignment, beam walking	Ø1" Broadband Dielectric Mirror (400–750 nm), mounts	Thorlabs (BB1-E02)	2
Telescope (Beam Expander)	T	Expands beam by factor 3	f = -100 mm (ACN254-100-A), f = 300 mm (AC254-300-A-ML)	Thorlabs (ACN254-100-A, AC254-300-A-ML)	1
Excitation filter	ExF	Cleans excitation light spectrally	25 mm bandpass filter (Quad Line ZET 405/488/561/640)	AHF (F59-405)	1
Mirror (3 & 4)	M	Reflects beam; alignment, beam walking	Ø2" Broadband Dielectric Mirror (400–750 nm)	Thorlabs (BB2-E02)	2
Tube lens (illumination)	TL_{ill}	Focuses beam into back focal plane of objective	f = 200 mm, Ø2" Achromatic Doublet (ACT508-200-A-ML)	Thorlabs (ACT508-200-A-ML)	1
Mirror (TIRF)	M	On translation mount for TIRF angle introduction	Ø2" Broadband Dielectric Mirror + stage (LNR25M/M)	Thorlabs (BB2-E02, LNR25M/M)	1
Dichroic mirror	DiM	Reflects excitation, transmits fluorescence	Quadband TIRF beamsplitter (zt405/488/561/640rpc)	AHF F73-410T3)	1
Objective lens	O	High NA lens for excitation and fluorescence collection	Nikon CFI Apo TIRF 60x, NA 1.49, Oil (MRD01691)	Nikon Nikon CFI Apo TIRF 60XC Oil)	1
Mirror	M	Reflects collected fluorescence to camera	Ø2" Broadband Dielectric Mirror (400–750 nm)	Thorlabs (BB2-E02)	1
Emission filter	EmF	Cleans emission light from laser back-reflections	Quad Line Rejectionband ZET405/488/561/640	AHF (F57-406)	1
Tube Lens (detection)	TL_{det}	Detection tube lens	f = 200 mm Tube Lens (TTL200-A)	Thorlabs (TTL200-A)	1
Camera	C	Records fluorescence	Andor Zyla 4.2 sCMOS	Andor (Andor Zyla 4.2 sCMOS)	1

2. PHASOR MAGNITUDE FITTING

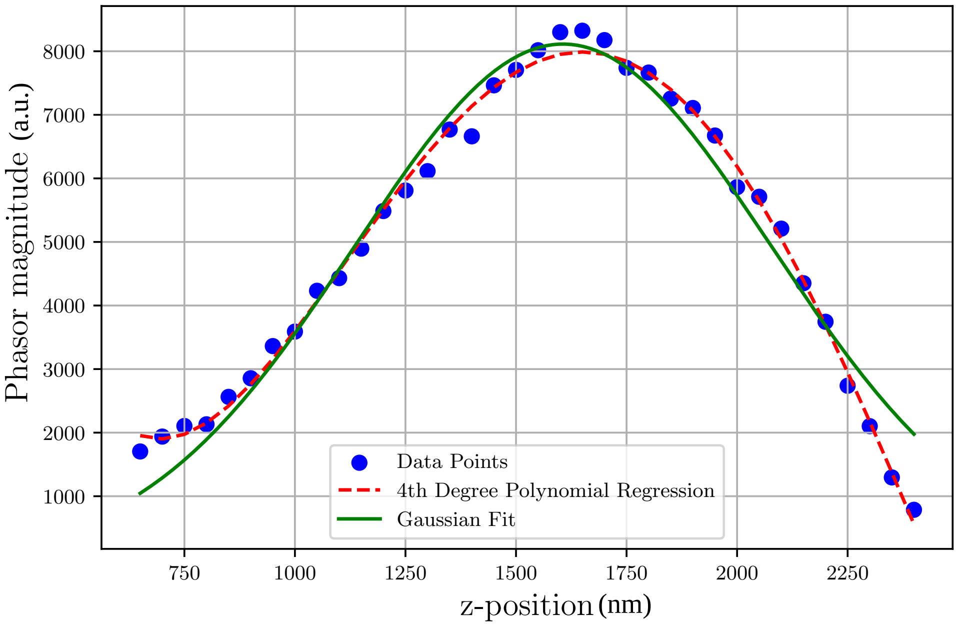

Fig. S2. Phasor magnitude fitting across a z-stack. Due to optical aberrations, the phasor magnitude of a single bead deviates from an ideal Gaussian profile. Although a fourth-degree polynomial provides a better fit, a Gaussian model is used to reduce computational complexity. Moreover, the polynomial fit is prone to overfitting, which can result in significant errors in the fitted profile.

3. SYSTEM IDENTIFICATION

If the dynamics of the drift are known, it becomes possible to design two key components: (1) an optimal filter that separates the true system dynamics from measurement noise, enabling accurate feedback control of the stage, and (2) a predictive model that anticipates future drift, allowing for preemptive control actions to minimize its effect.

A widely used framework for modeling such systems is the discrete-time LTI (Linear Time Invariant) state-space representation:

$$\boldsymbol{x}_{k+1} = A\boldsymbol{x}_k + B\boldsymbol{u}_k + w_k, \quad w_k \sim \mathcal{N}(0, Q) \tag{S1}$$

$$\boldsymbol{y}_k^m = C\boldsymbol{x}_k + D\boldsymbol{u}_k + v_k, \quad v_k \sim \mathcal{N}(0, R) \tag{S2}$$

where $\boldsymbol{x}_k \in \mathbb{R}^n$ is the state vector, $\boldsymbol{u}_k \in \mathbb{R}^m$ is the input (e.g., stage input), $\boldsymbol{y}_k^m \in \mathbb{R}^p$ is the measured output (e.g., focus position), and A, B, C, D are system matrices to be estimated. The terms w_k and v_k represent process and measurement noise, respectively.
Here we describe how the unknown subspaces, A, B, C, D and noise correlation matrices Q and R can be determined. By either subspace estimation methods such as: N4SID and PBSID$_{opt}$ or by making additional assumptions on the drift such that it can be described as a Brownian walk. In A we describe how input-output data is generated for system identification. In B we describe the different models and how hyperparameters for these models are chosen. Finally in C, we compare the different models.

A. Input-output data generation

Although our primary interest lies in characterizing the optical system's dynamics at the nanometer scale, utilizing input-output behavior directly at this scale is challenging due to significant measurement noise, denoted by $\sigma^m_{\Delta i}$ for each axis i. To ensure a sufficient signal-to-noise ratio and to maintain observable correlations between inputs and outputs, pseudo-random step excitation amplitudes were set to $u_i = 3\sigma^m_{\Delta i}$.

Furthermore, since the system does not exhibit autonomous stabilization, open-loop motion of the stage can cause the focal point to drift outside the optical system's operating range. To mitigate this, a proportional feedback controller was employed to maintain focus. However, the presence of feedback introduces correlations between the control inputs and the measured outputs, potentially biasing the system identification process. To reduce this effect, relatively small proportional gains were selected: $K_p = [0.05,\ 0.05,\ 0.1]$ for the $[x,\ y,\ z]$ axes, respectively. These gains were chosen to balance the need for stabilization with the goal of preserving the intrinsic system dynamics. As a result of the low feedback gains, the stabilization response was slower, requiring the step input intervals to be extended to 15 frames, roughly $1Hz$, to avoid exceeding the system's operational bounds. This only limits the identification of subspace matrix C between the inputs and the states but does not limit the identification of subspace matrix A. The piezo stage is assumed to act linear at higher frequency stage inputs up to 35Hz, as specifications of the used stage positioner indicate linear behaviour up until 1kHz. A representation of the inputs can be seen in Figure S6.

B. Model selection

We implemented three models to describe the system dynamics, listed here in order of increasing complexity: the identity model, the N4SID algorithm, and its closed-loop variant, the PBSID$_{\text{opt}}$ algorithm.

The *identity model* assumes that the system follows a pure Brownian motion. Under this assumption, the state-space matrices are defined as identity matrices, i.e., $A = B = C = I$, implying that the state evolves as a random walk without deterministic dynamics. The measurement noise covariance matrix R is estimated empirically by analyzing the displacement of beads over 100 consecutive frames, with the standard deviation used as a proxy for measurement noise level. The process noise covariance matrix Q is defined as:

$$Q = \begin{bmatrix} 10^q & 0 & 0 \\ 0 & 10^q & 0 \\ 0 & 0 & 10^q \end{bmatrix}, \tag{S3}$$

where q is a tunable scalar parameter that determines the magnitude of the process noise. The value of q was selected empirically by inspecting the filter response to various noise levels, as illustrated in Figure S3. A value of $q = -0.5$ was found to offer a suitable trade-off between noise suppression and responsiveness of the filtered signal.

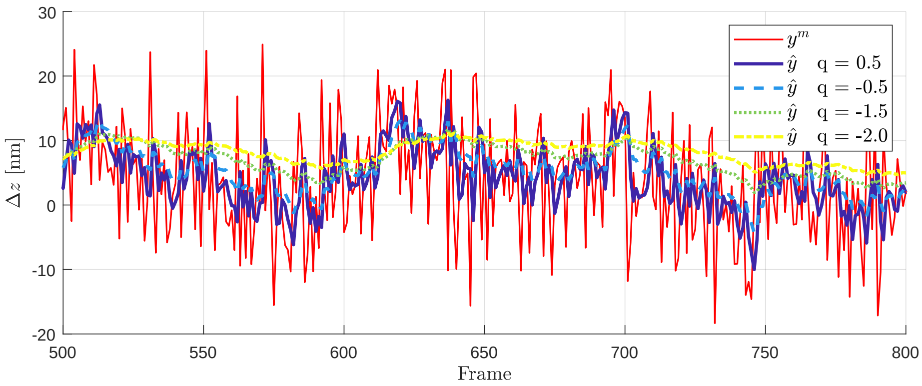

Fig. S3. Comparison of measured and estimated axial drift Δz. Increasing the process noise parameter q in the Kalman filter increases reliance on measurements, resulting in estimates that more closely track the observed data.

Making only use of the aforementioned identity model provides a simple baseline, but it does not capture any underlying deterministic behavior in the drift. To address this, we also explored

system identification methods, which aim to learn dynamic models directly from data. One widely used approach is the Numerical algorithms for Subspace State Space System Identification (N4SID) [1]. This method constructs a low-dimensional subspace from observed input-output data and uses it to estimate the system matrices A, B, C, D of a discrete-time state-space model. However as seen in A, inputs and process noise become correlated as the system is running closed-loop while generating system identification data, this correlation introduces bias in the identified model when standard open-loop identification methods such as N4SID are used. To address this, closed-loop subspace identification methods such as $\mathrm{PBSID}_{\mathrm{opt}}$ (Prediction-Based Subspace Identification with optimal weighting) can be employed. $\mathrm{PBSID}_{\mathrm{opt}}$ extends subspace identification to closed-loop conditions by incorporating a predictor form that explicitly accounts for the process noise [2, 3].
For both open-loop and closed-loop system identification, the past window size p in the block Hankel matrix must be appropriately selected. To identify the optimal value of p, the Akaike Information Criterion (AIC) was computed for various combinations of past window sizes and model orders. The AIC balances model fit and model complexity, enabling principled model selection [4].

The AIC is defined as:

$$\mathrm{AIC} = N \cdot \log \left(\det \left(\frac{1}{N} \sum_{t=1}^{N} \varepsilon(t,\hat{\theta})\varepsilon(t,\hat{\theta})^{\top} \right) \right) + 2n_p + N \cdot n_y \cdot (\log(2\pi) + 1) \tag{S4}$$

Here, N is the number of measurements in the dataset, $\varepsilon(t,\hat{\theta})$ is the $n_y \times 1$ vector of prediction errors at time t based on the estimated parameters $\hat{\theta}$, n_p is the number of estimated parameters in the model, and n_y is the number of model outputs. Based on the results presented in Figure S4, although the AIC stabilizes beyond a past window size of $p = 3$, we select $p = 6$ to allow flexibility for additional states, given the condition $n \leq p$ [3]. Similarly, the singular value plot shown in Figure S5 indicates that the singular values exhibit negligible jumps after model order 3, which implies that the main dynamics are captured within three states [5] . Therefore, in addition to the direct linear relationships between Δx, Δy, and Δz with the inputs, no higher-order linear dynamics can be reliably identified using subspace identification methods.

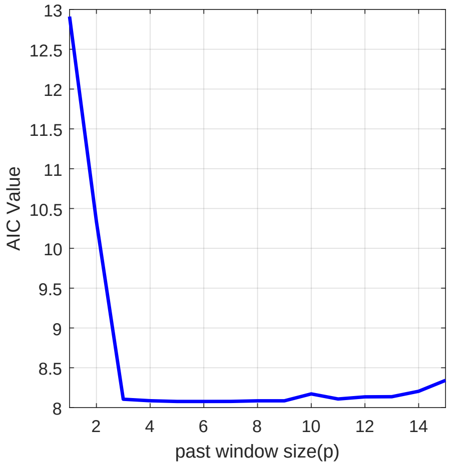

Fig. S4. AIC for different past window sizes, showing a minimum at $p = 6$.

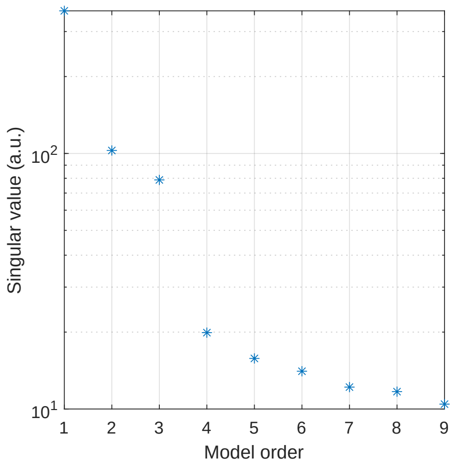

Fig. S5. Singular Value Plot, showing a big drop only after model order 3.

C. Model validation

After performing system identification, model quality is assessed using the Root-Mean-Squared-error metric,

$$\text{RMSE} = \sqrt{\frac{1}{n}\sum_{k=1}^{n}(\boldsymbol{y_k} - \boldsymbol{\hat{y}_k})^2}$$

A lower RMSE indicates that the model closely reproduces the observed behavior of the system, implying better predictive accuracy and a more faithful representation of the system dynamics. To determine the RMSE of the different models, we identified the model using N4SID and PBSID$_{opt}$ with training sets of 500 measurements. After which they were validated over the complete 2500 measurement dataset. The Identity model did not need training but used the same data set for validation.

Table S2. Mean and standard deviation of the Root Mean Squared Error over 5 system identifications, reported in nm for each model and axis. (Identity model is not identified using multiple training sets so has no standard deviation)

Model	**RMSE$_{\Delta x}$ (nm)**	**RMSE$_{\Delta y}$ (nm)**	**RMSE$_{\Delta z}$ (nm)**
Identity	0.62	1.1	2.8
N4SID	0.87 ± 0.058	1.2 ± 0.098	2.6 ± 0.087
PBSID$_{\text{opt}}$	0.90 ± 0.02	1.2 ± 0.12	2.6 ± 0.11

As shown in Table S2, the N4SID and PBSID$_{\text{opt}}$ models yield comparable RMSE values, indicating similar overall identification performance, indicating that the Closed-Loop data did not severely decrease model performance. Notably, the Identity model achieves a significantly lower RMSE in estimating Δ_x compared to both the other models and its own estimation of Δ_y. This outcome is unexpected, considering that Δ_x and Δ_y are measured using identical procedures. Additionally, the Identity model exhibits a slightly higher RMSE in estimating Δ_z, indicating a modest reduction in performance along that axis. The difference between the Δ_x and Δ_y estimation performance of the Identity model can be further understood by examining Figure S6, which displays the measured outputs, stage inputs, and state estimations for all three models. A detailed inspection of the data around frames 40 and 60 reveals a coupling effect between Δ_y and Δ_z. Specifically, for identical inputs in Δ_y, the system exhibits varying dynamic responses depending on the concurrent input in Δ_z. As the Identity model does not account for such cross-axis coupling, this limitation likely contributes to its comparatively poorer performance in estimating Δ_y relative to Δ_x. A plausible explanation for the observed coupling is a mechanical tilt in the piezoelectric stage along the x-axis, which causes the y-position of the bead projections on the camera to vary with changes in the z-axis position and vice versa, also explaining the poorer estimation of Δ_z. Such a tilt would be easily implementable in the Identity model by multiplying the B matrix with a rotational transformation matrix:

$$R_x(\theta) = \begin{bmatrix} 1 & 0 & 0 \\ 0 & \cos\theta & -\sin\theta \\ 0 & \sin\theta & \cos\theta \end{bmatrix}. \tag{S5}$$

Where θ must be found such that the RMSE are minimal. The identified models are not able to properly correlate the inputs to the outputs as the measured value rises more at each pseudo random input than the estimated states, but seems to identify the tilt. This causes Δ_x to be relatively worse than the identity model but Δ_y and Δ_z to perform similarly well as it benefits from identifying the tilt despite improper correlation of the inputs.

The identified models exhibit limited ability to accurately correlate the stage inputs with the measured outputs; the measured signals show larger increases in response to each pseudo-random input than are reflected in the estimated states, suggesting a systematic underestimation of the input magnitude. Despite this mismatch, the models effectively capture the underlying tilt present in the data, which appears to compensate for the poor input-output correlation. Consequently, while the estimation of Δ_x is degraded relative to the Identity model, the estimations of Δ_y and Δ_z remain comparable due to the benefit of capturing the tilt component.

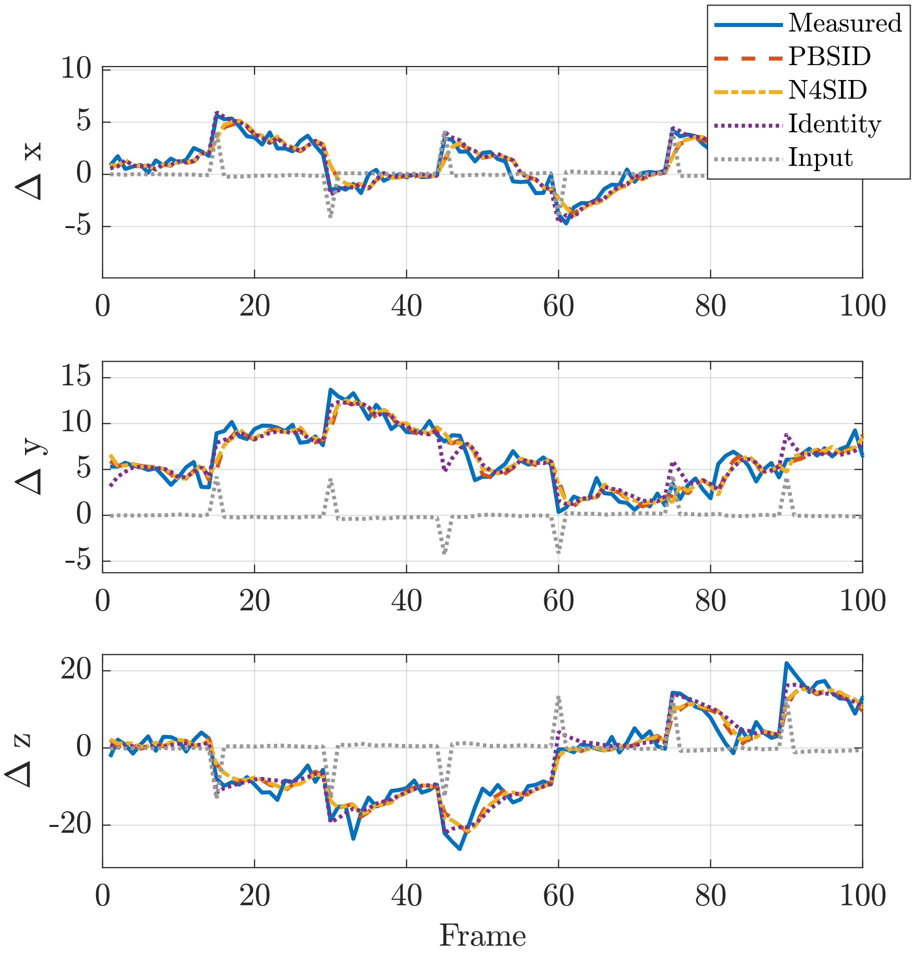

Fig. S6. Measured outputs and one step ahead predicted outputs of PBSID$_{opt}$, N4SID and Identity method first 100 frames of validation set.

Moreover, we perform residual analysis through the autocorrelation of the estimation error,$\boldsymbol{\epsilon}_k = \boldsymbol{y}_k - \hat{\boldsymbol{y}}_k$, and the cross-correlation between the error and inputs, $\boldsymbol{u}_k$. A well-identified model should yield a residual autocorrelation resembling a Dirac impulse, indicating that the residuals are white and that no significant system dynamics have been left unmodeled. Similarly, the absence of cross-correlation between past inputs and residuals implies that the model has adequately captured the input–output relationship.

Figure S7 illustrates that the autocorrelation of the residuals for both PBSID$_{\text{opt}}$ and N4SID remains within the 0.1 confidence bounds for nearly all time lags, with the exception of lag $\tau = 1$. This observation supports the earlier conclusion that the identified models underestimate the input magnitude, leading to residual correlations between consecutive frames. In such cases, the system appears to require an additional measurement step to fully adjust to changes in position. In contrast, the Identity model exhibits low residual autocorrelation for Δ_x even at lag $\tau = 1$, indicating a more immediate response. However, since the tilt is not explicitly modeled in the Identity case, a similar autocorrelation pattern to the identified models is observed for Δ_y and Δ_z, again suggesting that the system dynamics in these directions are not fully captured without incorporating cross-axis effects.

In Figure S8, the identified models exhibit similar cross-correlation behavior between the state estimation error and the control inputs, characterized by a pronounced peak at the initial lags followed by stabilization. This pattern reinforces the earlier observation that the models tend to underestimate the true state position. As a result, the residuals exhibit correlation with subsequent control inputs, which act to steer the system back toward the center of the operating region. This correlation is not observed for Δ_x and Δ_y in the Identity model, indicating that the residuals in these directions are largely uncorrelated with the control inputs. However, in the case of Δ_z, a negative correlation is present at lag $\tau = 1$, which may be attributed to the mechanical tilt discussed earlier. Specifically, an input to the z-stage appears to induce a coupled response, producing motion along the y-axis and a reduced displacement in the z-direction. This coupling leads to an estimation error in Δ_z that is inversely correlated with the subsequent control input.

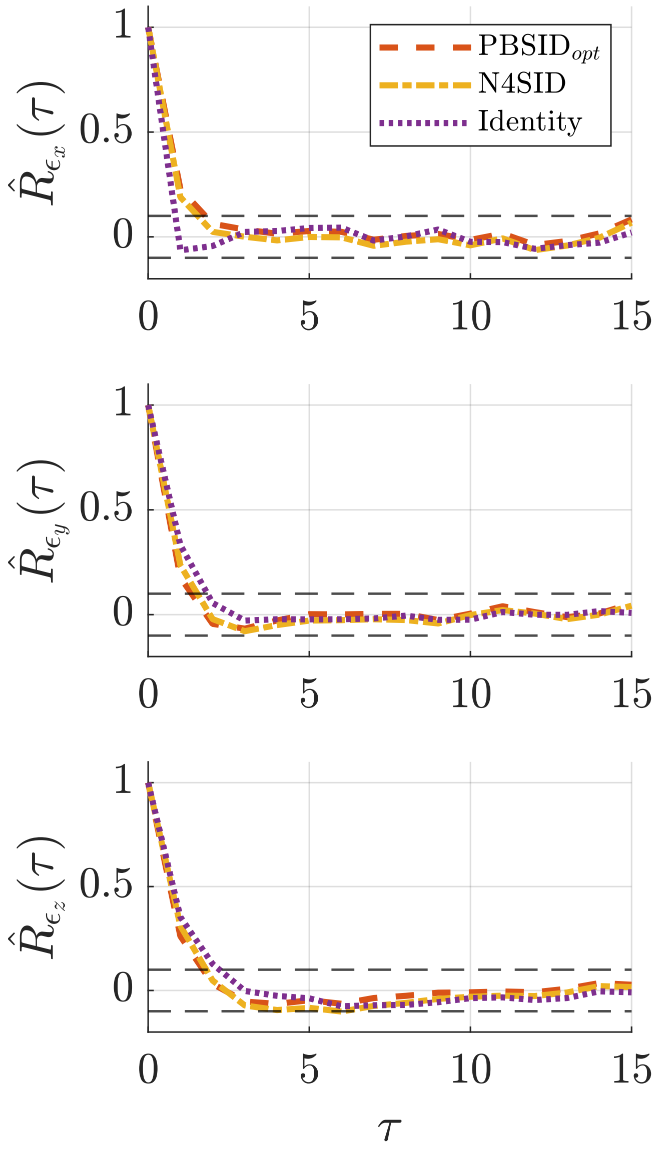

Fig. S7. Auto-correlation of the residuals of the different models. With 0.1 boundaries shown with black dashes. Frame lag τ is shown on the x-axis.

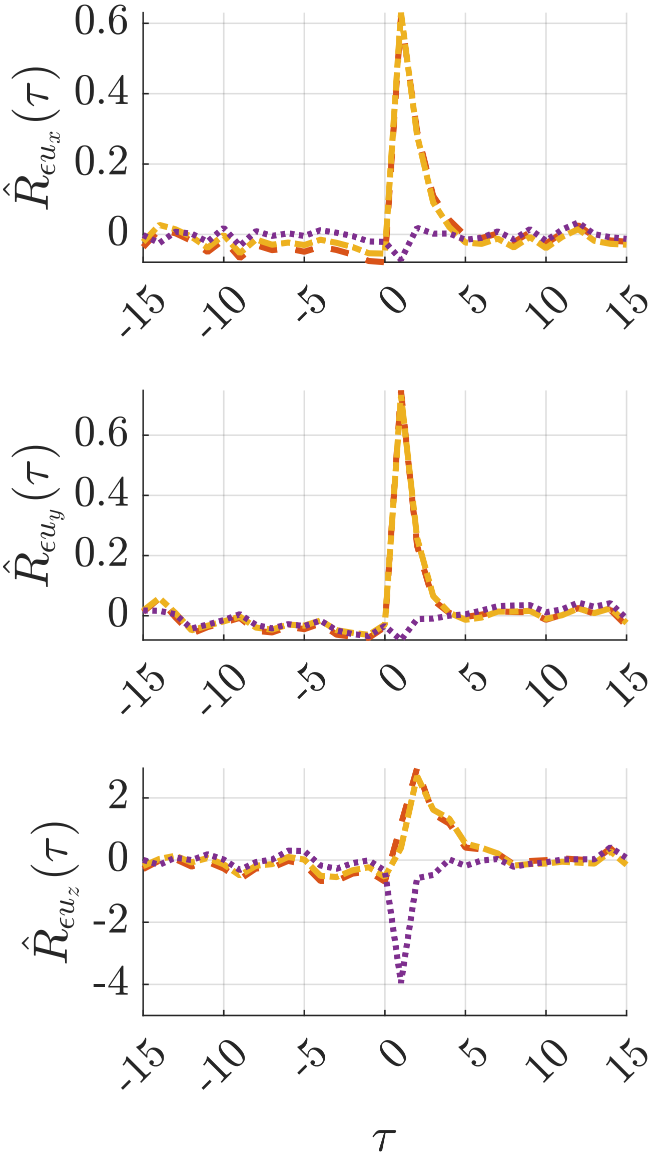

Fig. S8. Cross-correlation of the errors and input data of the different models. Frame lag τ is shown on the x-axis. Graphs correspond to legend in Figure S7.

4. CONSISTENCY OF BEAD EXCITATION

One limitation of using fiducial markers for axial drift estimation is the variability in the intensity of their fluorescence emission upon excitation. Since this intensity directly influences the phasor magnitude, fluctuations can introduce artifacts in the axial position estimate. Specifically, a change in phasor magnitude, may be misinterpreted as axial drift, prompting the stage to incorrectly apply a correction.

To investigate the stability of bead excitation and its impact on drift correction, a sample containing 0.5 μm Tetraspeck beads was prepared. Drift compensation was performed over a 50-minute period, during which a z-stack was acquired every 30 seconds. These z-stacks were analyzed to monitor changes in the Gaussian fits of the phasor magnitude over time, as shown in

Figure S9.

A closer inspection around the controlled focus position at 1180 nm in Figure S10 reveals fluctuations in bead excitation intensity, indicating non-uniform photostability. To quantify the effect of these fluctuations on axial position estimation, the fitted z-positions assuming a constant phasor magnitude were compared across time. The resulting residual drift after each new z-stack are presented in Figure S11, showing clear fluctuations.

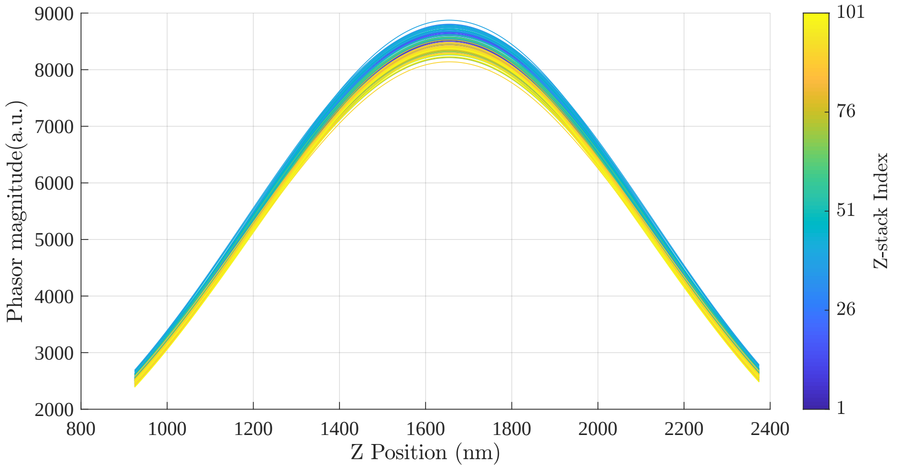

Fig. S9. Gaussian fits of 100 z-stacks over 50 minutes of a single bead's phasor magnitude.

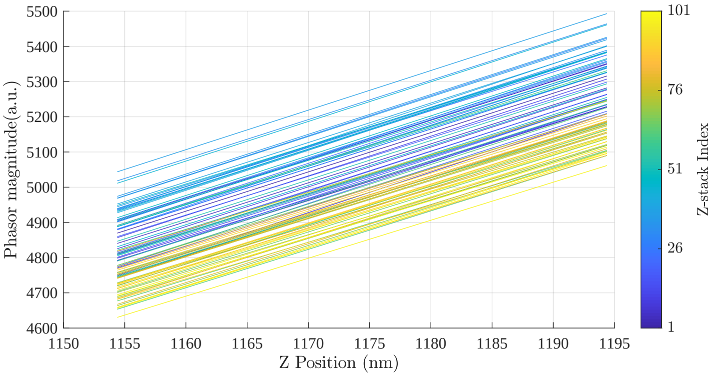

Fig. S10. Zoomed-in figure of S9 around desired focus point.

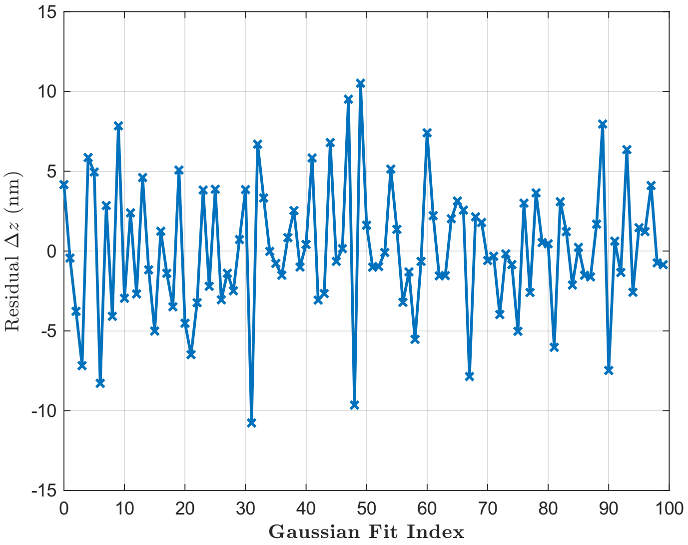

Fig. S11. Residual of the estimated axial focus position after each new Gaussian fit.

Photobleaching is an inherent photophysical property of fluorescent dyes that leads to a progressive loss of fluorescence emission, typically following an exponential decay. This phenomenon is the primary cause of the observed decrease in phasor magnitude over time. As the phasor magnitude diminishes, the estimated axial position, Δz is biased: when the focal plane is above the bead, the estimated Δz decreases, and when the bead lies above the focal plane, the estimated Δz increases. This is evident from Figure S2.

Since photobleaching is directly related to the excitation intensity, beads located further from the focal plane experience reduced photobleaching. Consequently, this spatial dependence leads to bead-specific deviations in the estimated Δz over time, as shown in Figure S12. In this experiment, seven 1 μm TetraSpeck beads were employed for drift correction. The final drift estimate was computed as the mean of the individual bead estimates. As a result, the individual Δz trajectories are centered around zero but show systematic deviations due to variations in photobleaching rates.

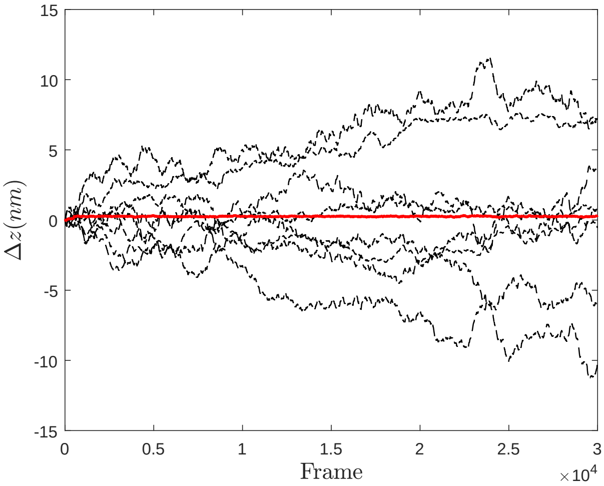

Fig. S12. Estimated axial drift (Δz) of seven fiducial beads over time during a single acquisition with live closed-loop control. A 1000-frame moving average was applied to reduce noise and emphasize long-term trends in the position estimation and bead excitation inconsistency. Black dotted: estimated Δz by different beads, red solid line: $\overline{\Delta z}$.

5. IMPLEMENTATION WORKFLOW OF THE DRIFT CORRECTION SYSTEM DURING SMLM ACQUISITION

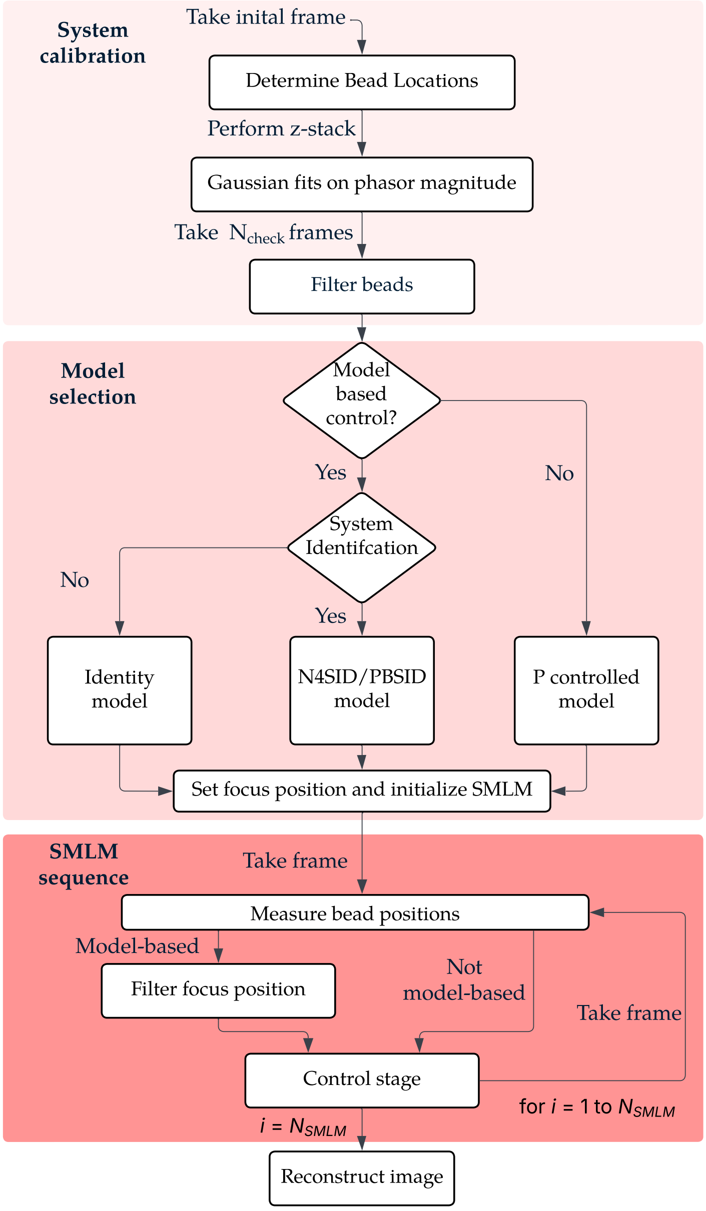

Fig. S13. Schematic overview of the imaging and drift correction workflow. The process begins with system calibration, where bead locations are identified from an initially captured frame. A z-stack is then acquired to generate Gaussian fits on the phasor magnitude, enabling 3D localization of all fiducial beads. Using N_{check} frames, the measurement noise for each bead is estimated, and beads exhibiting excessive noise are filtered out. In the subsequent model selection stage, the control method is chosen: either a proportional (P) controller or a model based controller using the identity model, which requires no system identification, or a model-based controller using N4SID or PBSIDopt, both of which require system identification. After selecting the control strategy, the user manually sets the initial focus position, and the SMLM acquisition begins. The chosen model is then used to filter the focus position and control the system states over NSMLM frames. The procedure concludes with image reconstruction.

Chapter 4

Conclusion

This chapter presents a summary of the key findings of this thesis. Section 4-1 provides an overview of the main contributions and results. Section 4-2 discusses the limitations of the experimental approach and the interpretation of the results. Moreover, it outlines potential directions for future research enabled by this work and suggests avenues for further development of drift correction methods for Single-Molecule Localization Microscopy (SMLM).

4-1 Summary

Super Resolution Microscopy (SRM) enables biologists to study structures and processes at the nanoscale, well below the diffraction limit of conventional light microscopy. By surpassing this fundamental resolution barrier, SRM allows precise visualization of molecular organization and dynamics that were previously inaccessible with standard optical techniques.

One such SRM method, SMLM, achieves super-resolution by localizing individual fluorescent molecules with high precision, provided their Point Spread Function (PSF)s do not overlap. This is enabled by photoswitching, where fluorophores stochastically blink between bright and dark states, allowing only a sparse subset to emit at any time. Thousands of sequential images are captured, and the positions of ON-state molecules are computed and compiled to reconstruct a high-resolution image beyond the diffraction limit. Without drift, localization precision is fundamentally bounded by the Cramér–Rao lower bound.

However, if drift occurs during the acquisition phase in SMLM, it degrades the precision of single-molecule localization by introducing an additional source of uncertainty. Specifically, the smallest possible variance of the estimated position, assuming CRLB can be reached, is given by $\mathrm{Var}(\hat{x}) = \sigma^2_{x,CRLB} + \mathrm{Var}(\Delta_x)$, where $\sigma^2_{x,CRLB}$ denotes the theoretical lower bound determined by the maximum likelihood estimator using the intensity of the molecules, background intensity information, PSF and camera pixel size [38]. $\mathrm{Var}(\Delta_x)$ represents the variance introduced by system drift. As a result, effective drift correction is essential to preserve the localization precision inherent to the imaging system. This requirement becomes increasingly critical with the emergence of advanced localization techniques such as MINFLUX, which approach the Cramér–Rao lower bound (CRLB) with nanometer or sub-nanometer precision [14]. In such high-precision regimes, even minor uncorrected drift can significantly compromise localization performance. Therefore, the development of precise and universally applicable drift correction methods is vital for enabling the full potential of cutting-edge single-molecule localization microscopy.

Although drift correction modules capable of nanometer precision are commercially available, they typically rely on the integration of additional microscope hardware. This often includes a secondary optical path equipped with at least one supplementary camera and an infrared laser, along with other necessary optical components to enable precise drift estimation. For many experimental setups, such modifications result in significant additional costs, which may not be feasible for all research groups. Furthermore, laboratories utilizing commercial microscope systems frequently encounter physical constraints that preclude the integration of a secondary optical path, making the implementation of such drift correction modules not only expensive but also physically impractical.

That is why this thesis focused on finding the answer to the research question: *"How can sample drift-induced resolution drop in SMLM be minimized using an actively controlled system that operates under typical SMLM constraints, enabling precise imaging in environments where computational resources are limited and modifications to the optical setup are not feasible?"*

The proposed solution requires only the inclusion of fluorescent fiducial markers in the sample, a sample preparation step that is commonly used in existing drift correction approaches and can be readily performed by biologists. Consequently, this method is non-invasive and fully compatible with standard super-resolution microscopy workflows. The fiducial markers could be excited using the same lasers, already present in most super-resolution microscope systems, and emit fluorescence that is detected by the same camera used for imaging single fluorophores. This eliminates the need for additional excitation sources or detection devices, thereby minimizing both cost and system complexity.

Since the fiducial markers were immobilized relative to the sample plane, their recorded PSFs could be used to infer any relative displacement between the sample and the focal plane. Estimating this displacement required determining the marker positions from their image data. A computationally efficient method for doing this was the Phasor approach, which used the phase angles of the $(1,0)$ and $(0,1)$ Fourier coefficients to estimate lateral displacements and their magnitudes to estimate axial shifts. By averaging measurements from multiple fiducial markers, measurement noise was reduced. However, the number of usable markers is constrained by the camera's field of view. To further enhance drift estimation precision under such limitations, a Kalman filter was employed. To enable Kalman filtering, this thesis also investigated the development of a suitable dynamical model of the drift process.

Three models were evaluated. First, the Identity model assumed that the drift follows a Brownian motion and could be described solely by characterizing the process and measurement noise. Second, the open-loop system identification method Numerical Algorithms for Subspace State Space System Identification (N4SID) was employed to capture potential underlying drift dynamics by recording drift trajectories at 30 Hz over the course of one minute. Finally, recognizing that fiducial markers emit sufficient photons to resolve axial drift only within a limited range, the measurements were used in a closed-loop feedback configuration to stabilize the focal plane. In this scenario, the correlation between noise and input introduces bias into standard identification methods. To mitigate this, the closed-loop identification method Predictor-Based Subspace IDentification optimal (PBSID$_{opt}$) was also applied.

Model validation metrics were compared using the autocorrelation of the error between measured and estimated outputs over time, as well as the cross-correlation between the error and the input. These comparisons between open-loop and closed-loop system identification methods revealed no significant differences. Further results showed that only minor system asymmetries, specifically, slight stage misalignments causing correlation between y- and z-axis measurements, could be detected using the identification procedures. These small couplings led to modest improvements in the identified models. However, the input magnitude was underestimated during model identification, leading to a mismatch between the modeled and actual system response. As a result, only the x-axis estimation performance, determined as the RMSE between the measured output and estimated output, of the Identity model (0.62 nm) was significantly lower than for the identified models N4SID (0.87 nm) and PBSID$_{opt}$ (0.9 nm). For the y- and z-axes, the RMSE values were approximately the same across all models, as the modest improvements gained from capturing coupling effects in the identified models were counteracted by the Identity model not suffering from input magnitude underestimation. No other significant deterministic dynamics were observed, and the final state-space model retained a minimal structure with three independent states, each corresponding to a spatial axis and influenced solely by stochastic drift.

4-2 Discussion and Future Work

4-2-1 Bead Selection and Stability

The choice and stability of fiducial beads were found to be critical for precise drift correction. While gold nanoparticles were initially considered, they proved highly unstable when used as fluorescent markers. Consequently, fluorescent beads were selected. Bead size played a significant role in localization precision: larger beads exhibit reduced photobleaching and higher signal-to-noise ratios, improving localization precsion. However, they also occupy more space in the field of view. In the used experimental setup, a size of 1 μm was determined to be optimal, balancing visibility, precision, and minimal spatial intrusion.

Color selection was equally important. To ensure precise multi-channel imaging, the emission wavelength of the fiducial beads had to be sufficiently separated from the single-molecule signal. This allowed for effective spectral separation and channel-specific regulation.

4-2-2 Fitting Accuracy and Model Limitations

In this work, a Gaussian model was used to fit the bead point spread function (PSF), despite the presence of optical aberrations. While this approach is computationally efficient and robust in many conditions, it may not fully capture PSF distortions introduced by aberrations. In certain cases, higher-order polynomial models or physically-motivated PSF models may offer improved fitting accuracy at the cost of increased computational complexity. In particular, fitting aberration-specific polynomials could yield better results [40].

4-2-3 Bleaching-Induced Drift Artifacts

Photobleaching of fiducial beads presented a significant source of error in drift estimation. As the beads bleach, the emitted photon count decreases, which can be misinterpreted by the fitting algorithm as a spatial displacement, thus inducing a false drift signal. To mitigate this effect, low laser powers and pre-bleaching strategies were employed, as recommended in [2]. Nonetheless, bleaching effects remained a concern due to the dependence of excitation efficiency on axial position and lateral illumination inhomogeneities, despite the use of a PiShaper beam shaper to turn the Gaussian excitation beam into a tophat.

To compensate for bleaching-related artifacts, intermittent z-stacking was used to model and correct for intensity changes. However, fluctuations in laser power occasionally led to poorly fitted intensity profiles, introducing bias and reducing the robustness of the correction.

Future work could explore methods to detect and compensate for bleaching more systematically. One promising approach involves positioning fiducial beads both above and below the focal plane. Due to the asymmetry in the PSF and its phasor magnitude response, bleaching-induced intensity loss would cause opposite estimation shifts depending on the bead's axial position: beads below the focus plane would appear lower than their true position, while beads above would appear higher. By analyzing the divergence of these estimates, it may be possible to detect and quantify bleaching. This information can be used to adjust the measured data accordingly, allowing the affected beads to remain usable for drift estimation while compensating for the bleaching-induced error.

4-2-4 Limitations of System Identification

Due to photobleaching effects, the input-output dataset was limited to 500 samples acquired at 30 Hz to minimize bias in the system identification caused by bleaching-induced virtual drift. As a result, the identification process was primarily sensitive to high-frequency dynamics. Under these constraints, no significant system dynamics were detected, aside from indications of possible stage misalignment. In optical systems equipped with high-speed, hardware-based tracking methods capable of higher temporal resolution and precision, it is likely that additional dynamic components, such as vibrations induced by electronic interference, could be observed and reliably identified using system identification techniques.

Low-frequency processes such as thermally induced drift were not adequately captured because of the relatively small amount of data. However, during extended acquisition periods exceeding one hour, a recurring drift pattern was observed, which appeared to correlate with the activation cycle of the local HVAC system. Similar correlation between ambient temperature and drift was seen previously in [39]. To better capture and compensate for low-frequency drift, future work could incorporate ambient temperature measurements, for example by integrating a temperature sensor into the setup. This would allow correlation analysis between temperature fluctuations and the estimated drift states. Identifying such relationships could enable model-based compensation for thermally induced drift, improving long-term stability in prolonged acquisitions.

Appendix A

Derivation PBSID$_{opt}$

The algorithm is similar to what is done in the open-loop Numerical algorithm for the Subspace State Space System IDentification (N4SID) class of algorithms [42]. The following derivation is conducted according to [41]. First Eq. 2-1 is extended and rewritten as,

$$\boldsymbol{x_{t+1}} = \tilde{A}\boldsymbol{x_t} + \tilde{B}\boldsymbol{u_t} + L\boldsymbol{y_t^m} \tag{A-1}$$

$$\boldsymbol{y_t^m} = C\boldsymbol{x_t} + v_t, \quad v_t \sim \mathcal{N}(0, R), \tag{A-2}$$

where $\tilde{A} \equiv A - CL$ and $\tilde{B} \equiv B - LD$. Here matrix L is the Kalman observer gain with which it is assumed that the pair (A, C) is observable and has eigenvalues inside the unit circle and the pair $(A, [B \;\, LR^{\frac{1}{2}}])$ is reachable, where R is the covariance matrix of the measurement noise. Some extra notation has to be declared before deriving the estimation of the Markov parameters, needed for N4SID. A new stacked vector $\boldsymbol{\zeta_t}$ defined as, $\boldsymbol{\zeta_t} = \begin{bmatrix} \boldsymbol{u_t} \\ \boldsymbol{y_t^m} \end{bmatrix}$, makes it possible to write down,

$$\boldsymbol{\zeta_t^{(p)}} = \begin{bmatrix} \boldsymbol{\zeta_{t-p}^T}, & \boldsymbol{\zeta_{t-p+1}^T}, & \ldots, & \boldsymbol{\zeta_{t-1}^T} \end{bmatrix}^T \tag{A-3}$$

where p denotes the past window size. Besides that, a reversed extended controllability matrix $\tilde{\mathcal{K}}^{(p)}$ is defined as,

$$\tilde{\mathcal{K}}^{(p)} = [\tilde{A}^{p-1}\bar{B}, \; \tilde{A}^{p-2}\bar{B}, \; \ldots, \; \bar{B}] \tag{A-4}$$

where $\bar{B} = [\tilde{B}, \; K]$. With these new notations the data equation common to many closed-loop subspace algorithms can be derived. The propagation in time in Eq. A-1 can be redefined with some initial state $\boldsymbol{x_k}$ as,

$$\boldsymbol{x_{k+p}} = \tilde{A}^p\boldsymbol{x_k} + \tilde{\mathcal{K}}^{(p)}\boldsymbol{\zeta_{k+p}^{(p)}}. \tag{A-5}$$

The new notations also make it be possible to rewrite Eq. A-2 as,

$$\boldsymbol{y_{k+p}^m} = C\tilde{A}^p\boldsymbol{x_k} + C\tilde{\mathcal{K}}^{(p)}\boldsymbol{\zeta_{k+p}^{(p)}} + v_{k+p}. \tag{A-6}$$

By the previously stated assumption that $\tilde{A}$ has all its eigenvalues inside the open unit disc, the term $\tilde{A}^p$ can be made arbitrarily small, which gives, $||\tilde{A}^p||_2 \simeq 0$ by choosing p sufficiently large. Hereby, a new set $\boldsymbol{Y_{p,N_p}}$ can be constructed, where N_p is defined as $N_p = N - p$ which consists of the expressions for y_p up to y_{N-1}, resulting in

$$\boldsymbol{Y_{p,N_p}} = C\tilde{\mathcal{K}}\boldsymbol{Z}_{0,p,N_p} + \boldsymbol{E}_{p,N_p}, \tag{A-7}$$

Where $\boldsymbol{E}_{p,N_p}$ is used to define the set of measurement errors. Here the block Hankel matrix is also introduced for $\boldsymbol{Z}_{0,p,N_p}$, which is constructed from data sequences as,

$$\boldsymbol{Z}_{i,p,N_p} = \begin{bmatrix} \zeta_i & \zeta_{i+1} & \cdots & \zeta_{i+N-p-1} \\ \zeta_{i+1} & \zeta_{i+2} & \cdots & \zeta_{i+N-p} \\ \vdots & \vdots & \ddots & \vdots \\ \zeta_{i+p-1} & \zeta_{i+p} & \cdots & \zeta_{i+N-p+p-2} \end{bmatrix} \tag{A-8}$$

With Eq. A-7 it is now possible to estimate the predictor Markov parameters [31]. The Markov parameters are found as performed in [41], by solving the Frobenius norm least squares problem,

$$\min_{C\tilde{\mathcal{K}}^{(p)}} \left\| \boldsymbol{Y}_{p,N_p} - [C\tilde{\mathcal{K}}][\boldsymbol{Z}_{0,p,N_p}] \right\|_F^2 . \tag{A-9}$$

When the data matrix, $\boldsymbol{Z}_{0,p,N_p}$, is full-rank, the least squares solution is found by calculating the RQ factorization of the following stacked data matrices,

$$\begin{bmatrix} \boldsymbol{Z}_{0,p,N_p} \\ \boldsymbol{Y}_{p,N_p} \end{bmatrix} = \begin{bmatrix} R_{11} & 0 \\ R_{21} & R_{22} \end{bmatrix} \begin{bmatrix} Q_1 \\ Q_2 \end{bmatrix} \tag{A-10}$$

By using back-substitution it can be found that an estimate of the Markov parameters $\widehat{C\tilde{\mathcal{K}}^{(p)}}$ can be found from

$$R_{21} = \widehat{C\tilde{\mathcal{K}}^{(p)}} R_{11}. \tag{A-11}$$

Now it will be shown how the Markov parameters in the estimated controllability matrix, $\widehat{C\tilde{\mathcal{K}}^{(p)}}$ can be used together with the extended observability matrix,

$$\tilde{\Gamma}^{(f)} = \begin{bmatrix} C \\ C\tilde{A} \\ \vdots \\ C\tilde{A}^{f-1} \end{bmatrix}, \tag{A-12}$$

to construct the observability-times-controllability matrix $\tilde{\Gamma}^{(f)}\tilde{\mathcal{K}}^{(p)}$ with future window $f > n$, n being the total amount of identified states.

$$\tilde{\Gamma}^{(f)}\tilde{\mathcal{K}}^{(p)} = \begin{bmatrix} C\tilde{A}^{p-1}\bar{B} & C\tilde{A}^{p-2}\bar{B} & \cdots & C\bar{B} \\ C\tilde{A}^{p}\bar{B} & C\tilde{A}^{p-1}\bar{B} & \cdots & C\tilde{A}\bar{B} \\ \vdots & \vdots & \ddots & \vdots \\ C\tilde{A}^{p+f-2}\bar{B} & C\tilde{A}^{p+f-3}\bar{B} & \cdots & C\tilde{A}^{f-1}\bar{B} \end{bmatrix} \tag{A-13}$$

Because of the earlier assumption that, $||\tilde{A}^p||_2 \simeq 0$, the observability-times-controllability matrix can be reduced to,

$$\tilde{\Gamma}^{(f)}\tilde{\mathcal{K}}^{(p)} \approx \begin{bmatrix} C\tilde{A}^{p-1}\bar{B} & C\tilde{A}^{p-2}\bar{B} & \cdots & C\bar{B} \\ 0 & C\tilde{A}^{p-1}\bar{B} & \cdots & C\tilde{A}\bar{B} \\ \vdots & \ddots & \ddots & \vdots \\ 0 & \cdots & 0 & C\tilde{A}^{f-1}\bar{B} \end{bmatrix} = C\tilde{\mathcal{K}}^{(p)}. \tag{A-14}$$

Thus, an estimation for $\tilde{\Gamma}^{(f)}\tilde{\mathcal{K}}^{(p)}$ can be found using the estimated Markov parameters. From A-1, it can be deducted that ignoring the first term, the product $\tilde{\mathcal{K}}^{(p)}\boldsymbol{Z}_{0,p,N_p}$ represents the state sequence $\boldsymbol{X}_{p,N_p}$. By definition, the product $\tilde{\Gamma}^{(f)}\tilde{\mathcal{K}}^{(p)}\boldsymbol{Z}_{0,p,N_p}$ equals to the observability matrix times the state sequence, $\tilde{\Gamma}^{(f)}\boldsymbol{X}_{p,N_p}$. With this a Singular Value Decomposition (SVD) can be performed,

$$\tilde{\Gamma}^{(f)}\boldsymbol{X}_{p,N_p} = \tilde{\Gamma}^{(f)}\tilde{\mathcal{K}}^{(p)}\boldsymbol{Z}_{0,p,N_p} = \widehat{C\tilde{\mathcal{K}}^{(p)}}\boldsymbol{Z}_{0,p,N_p} = \mathcal{U}_n\Sigma_n\mathcal{V}_n^T \tag{A-15}$$

After which the state sequence can be found from,

$$\hat{\boldsymbol{X}}_{p,N_p} = \Sigma_n\mathcal{V}_n^T. \tag{A-16}$$

The SVD in Eq. A-15, can also be used to determine the amount of states that the plant can be described with. For a perfect LTI system the amount of states n would equal the amount of non-zero singular values, however as the SVD is recovered from an estimate of the Markov parameters, this will not necessarily be true. The size of the past and future window affects the variance of the system's pole locations.

Finally, solving two least-squares problems can determine the state space matrices. The state-space equations in A-1 and A-2 can be rewritten in their respective data equation form as,

$$\boldsymbol{X}_{p+1,N_p-1} = \begin{bmatrix} A & B & L \end{bmatrix} \begin{bmatrix} \hat{\boldsymbol{X}}_{p,N_p-1} \\ \boldsymbol{U}_{p,N_p-1} \\ \boldsymbol{E}_{p,N_p-1} \end{bmatrix} \tag{A-17}$$

$$\boldsymbol{Y}_{p,N_p} = C\hat{\boldsymbol{X}}_{p,N_p} + \boldsymbol{E}_{p,N_p}. \tag{A-18}$$

Instead of first determining the state-space matrices A, B, C, D and then estimating the process and measurement noise covariance matrices Q and R simultaneously, as is typically done in N4SID, PBSIDopt proceeds differently. First, a least-squares solution to Eq. A-18 is used to estimate C and the innovation sequence $\boldsymbol{E}_{p,N_p}$. This estimated innovation is then substituted into Eq. A-17, allowing for a second least-squares problem to estimate A, B, and L. By explicitly modeling and isolating the innovations, which are uncorrelated with past inputs, PBSIDopt avoids the input-noise correlation issue that biases estimates in closed-loop identification scenarios.

Bibliography

[1] Paolo Annibale, Marco Scarselli, Mattia Greco, and Aleksandra Radenovic. Identification of the factors affecting co-localization precision for quantitative multicolor localization microscopy. *Optical Nanoscopy*, 1(1):9, 2012.

[2] Alexander Balinovic, David Albrecht, and Ulrike Endesfelder. Spectrally red-shifted fluorescent fiducial markers for optimal drift correction in localization microscopy. *Journal of Physics D: Applied Physics*, 52(20):204002, 2019.

[3] Eric Betzig, George H Patterson, Rachid Sougrat, O Wolf Lindwasser, Scott Olenych, Juan S Bonifacino, Michael W Davidson, Jennifer Lippincott-Schwartz, and Harald F Hess. Imaging intracellular fluorescent proteins at nanometer resolution. *science*, 313(5793):1642–1645, 2006.

[4] Pierre Bon, Nicolas Bourg, Sandrine Lécart, Serge Monneret, Emmanuel Fort, Jérôme Wenger, and Sandrine Lévêque-Fort. Three-dimensional nanometre localization of nanoparticles to enhance super-resolution microscopy. *Nature Communications*, 6(1), July 2015.

[5] Michael K Cheezum, William F Walker, and William H Guilford. Quantitative comparison of algorithms for tracking single fluorescent particles. *Biophysical journal*, 81(4):2378–2388, 2001.

[6] Shih-Ya Chen, Rainer Heintzmann, and Christoph Cremer. Sample drift estimation method based on speckle patterns formed by backscattered laser light. *Biomedical Optics Express*, 10(12):6462, November 2019.

[7] Ekta Seth Chhabra and Henry N Higgs. The many faces of actin: matching assembly factors with cellular structures. *Nature cell biology*, 9(10):1110–1121, 2007.

[8] Alessandro Chiuso. On the relation between cca and predictor-based subspace identification. *IEEE Transactions on Automatic Control*, 52(10):1795–1812, 2007.

[9] Jelmer Cnossen, Tao Ju Cui, Chirlmin Joo, and Carlas Smith. Drift correction in localization microscopy using entropy minimization. *Opt. Express*, 29(18):27961–27974, Aug 2021.

[10] Simao Coelho, Jongho Baek, Matthew S. Graus, James M. Halstead, Philip R. Nicovich, Kristen Feher, Hetvi Gandhi, J. Justin Gooding, and Katharina Gaus. Ultraprecise single-molecule localization microscopy enables in situ distance measurements in intact cells. *Science Advances*, 6(16), 2020.

[11] Gerald Donnert, Jan Keller, Rebecca Medda, M Alexandra Andrei, Silvio O Rizzoli, Reinhard Lührmann, Reinhard Jahn, Christian Eggeling, and Stefan W Hell. Macromolecular-scale resolution in biological fluorescence microscopy. *Proceedings of the National Academy of Sciences*, 103(31):11440–11445, 2006.

[12] Ahmed Elmokadem and Ji Yu. Optimal drift correction for superresolution localization microscopy with bayesian inference. *Biophysical Journal*, 109(9):1772–1780, 2015.

[13] Mats GL Gustafsson. Surpassing the lateral resolution limit by a factor of two using structured illumination microscopy. *Journal of microscopy*, 198(2):82–87, 2000.

[14] Klaus C Gwosch, Jasmin K Pape, Francisco Balzarotti, Philipp Hoess, Jan Ellenberg, Jonas Ries, and Stefan W Hell. Minflux nanoscopy delivers 3d multicolor nanometer resolution in cells. *Nature methods*, 17(2):217–224, 2020.

[15] Aleksandar Haber. Subspace identification of temperature dynamics. *arXiv preprint arXiv:1908.02379*, 2019.

[16] Aleksandar Haber, John E Draganov, and Michael Krainak. Subspace identification of low-dimensional structural-thermal-optical-performance (stop) models of reflective optics. In *Optical Modeling and Performance Predictions XII*, volume 12215, pages 39–54. SPIE, 2022.

[17] Mike Heilemann, Sebastian Van De Linde, Mark Schüttpelz, Robert Kasper, Britta Seefeldt, Anindita Mukherjee, Philip Tinnefeld, and Markus Sauer. Subdiffraction-resolution fluorescence imaging with conventional fluorescent probes. *Angewandte Chemie-International Edition*, 47(33), 2008.

[18] Stefan Hell and Ernst H. K. Stelzer. Properties of a 4pi confocal fluorescence microscope. *J. Opt. Soc. Am. A*, 9(12):2159–2166, Dec 1992.

[19] Ricardo Henriques, Mickael Lelek, Eugenio F Fornasiero, Flavia Valtorta, Christophe Zimmer, and Musa M Mhlanga. Quickpalm: 3d real-time photoactivation nanoscopy image processing in imagej. *Nature methods*, 7(5):339–340, 2010.

[20] Samuel T Hess, Thanu PK Girirajan, and Michael D Mason. Ultra-high resolution imaging by fluorescence photoactivation localization microscopy. *Biophysical journal*, 91(11):4258–4272, 2006.

[21] Bo Huang, Wenqin Wang, Mark Bates, and Xiaowei Zhuang. Three-dimensional super-resolution imaging by stochastic optical reconstruction microscopy. *Science*, 319(5864):810–813, 2008.

[22] Caroline Kulcsár, Henri-François Raynaud, Cyril Petit, Jean-Marc Conan, and Patrick Viaris de Lesegno. Optimal control, observers and integrators in adaptive optics. *Optics express*, 14(17):7464–7476, 2006.

[23] Xueming Li, Paul Mooney, Shawn Zheng, Christopher R Booth, Michael B Braunfeld, Sander Gubbens, David A Agard, and Yifan Cheng. Electron counting and beam-induced motion correction enable near-atomic-resolution single-particle cryo-em. *Nature Methods*, 10(6):584–590, May 2013.

[24] Hongqiang Ma, Maomao Chen, Phuong Nguyen, and Yang Liu. Toward drift-free high-throughput nanoscopy through adaptive intersection maximization. *Science Advances*, 10(21):eadm7765, 2024.

[25] Hongqiang Ma, Jianquan Xu, Jingyi Jin, Yi Huang, and Yang Liu. A simple marker-assisted 3d nanometer drift correction method for superresolution microscopy. *Biophysical Journal*, 112(10):2196–2208, May 2017.

[26] Koen J. A. Martens, Arjen N. Bader, Sander Baas, Bernd Rieger, and Johannes Hohlbein. Phasor based single-molecule localization microscopy in 3D (pSMLM-3D): An algorithm for MHz localization rates using standard CPUs. *The Journal of Chemical Physics*, 148(12):123311, 12 2017.

[27] Luciano A Masullo, Alan M Szalai, Lucía F Lopez, Mauricio Pilo-Pais, Guillermo P Acuna, and Fernando D Stefani. An alternative to minflux that enables nanometer resolution in a confocal microscope. *Light: Science & Applications*, 11(1):199, 2022.

[28] Philip R Nicovich, Dylan M Owen, and Katharina Gaus. Turning single-molecule localization microscopy into a quantitative bioanalytical tool. *Nature protocols*, 12(3):453–460, 2017.

[29] Raimund J Ober, Sripad Ram, and E Sally Ward. Localization accuracy in single-molecule microscopy. *Biophysical journal*, 86(2):1185–1200, 2004.

[30] Sanket Patil, Giuseppe Vicidomini, and Eli Slenders. Open-source 3d active sample stabilization for fluorescence microscopy. *bioRxiv*, pages 2025–01, 2025.

[31] Minh Phan, Jer-Nan Juang, and Richard W Longman. On markov parameters in system identification. Technical report, 1991.

[32] Thomas D Pollard and Gary G Borisy. Cellular motility driven by assembly and disassembly of actin filaments. *Cell*, 112(4):453–465, 2003.

[33] Amir Rahmani, Tabitha Cox, Akhila Thamaravelil Abhimanue Achary, and Aleks Ponjavic. Astigmatism-based focus stabilisation with universal objective lens compatibility, extended operating range and nanometre precision. *bioRxiv*, 2024.

[34] Michael J Rust, Mark Bates, and Xiaowei Zhuang. Sub-diffraction-limit imaging by stochastic optical reconstruction microscopy (storm). *Nature methods*, 3(10):793–796, 2006.

[35] Lothar Schermelleh, Alexia Ferrand, Thomas Huser, Christian Eggeling, Markus Sauer, Oliver Biehlmaier, and Gregor PC Drummen. Super-resolution microscopy demystified. *Nature cell biology*, 21(1):72–84, 2019.

[36] Roman Schmidt, Tobias Weihs, Christian A. Wurm, Isabelle Jansen, Jasmin Rehman, Steffen J. Sahl, and Stefan W. Hell. Minflux nanometer-scale 3d imaging and microsecond-range tracking on a common fluorescence microscope. *Nature Communications*, 12(1), March 2021.

[37] Mingtao Shang, Zhen li Huang, and Yujie Wang. Influence of drift correction precision on super-resolution localization microscopy. *Appl. Opt.*, 61(13):3516–3522, May 2022.

[38] Carlas S Smith, Nikolai Joseph, Bernd Rieger, and Keith A Lidke. Fast, single-molecule localization that achieves theoretically minimum uncertainty. *Nature methods*, 7(5):373–375, 2010.

[39] Xiaofan Sun, Zhengyi Zhan, Chenying He, Xin Luo, Yubing Han, Chuankang Li, Cuifang Kuang, and Xu Liu. Nanodriftguard: Open-source isotropic ångström-scale active stabilization for super-resolution microscopy. *Optics and Lasers in Engineering*, 190:108957, 2025.

[40] Rasmus Ø Thorsen, Christiaan N Hulleman, Mathias Hammer, David Grünwald, Sjoerd Stallinga, and Bernd Rieger. Impact of optical aberrations on axial position determination by photometry. *Nature methods*, 15(12):989–990, 2018.

[41] Gijs Van der Veen, Jan-Willem van Wingerden, Marco Bergamasco, Marco Lovera, and Michel Verhaegen. Closed-loop subspace identification methods: an overview. *IET Control Theory & Applications*, 7(10):1339–1358, 2013.

[42] Peter Van Overschee and Bart De Moor. N4sid: Subspace algorithms for the identification of combined deterministic-stochastic systems. *Automatica*, 30(1):75–93, 1994.

[43] Lexy von Diezmann, Yoav Shechtman, and W. E. Moerner. Three-dimensional localization of single molecules for super-resolution imaging and single-particle tracking. *Chemical Reviews*, 117(11):7244–7275, February 2017.

[44] Yina Wang, Joerg Schnitzbauer, Zhe Hu, Xueming Li, Yifan Cheng, Zhen-Li Huang, and Bo Huang. Localization events-based sample drift correction for localization microscopy with redundant cross-correlation algorithm. *Opt. Express*, 22(13):15982–15991, Jun 2014.

[45] Michael Weber, Marcel Leutenegger, Stefan Stoldt, Stefan Jakobs, Tiberiu S Mihaila, Alexey N Butkevich, and Stefan W Hell. Minsted fluorescence localization and nanoscopy. *Nature photonics*, 15(5):361–366, 2021.

[46] Yu-Le Wu, Aline Tschanz, Leonard Krupnik, and Jonas Ries. Quantitative data analysis in single-molecule localization microscopy. *Trends in Cell Biology*, 30(11):837–851, 2020.

[47] Ke Xu, Hazen P Babcock, and Xiaowei Zhuang. Dual-objective storm reveals three-dimensional filament organization in the actin cytoskeleton. *Nature methods*, 9(2):185–188, 2012.